Results in Optics 24 (2026) 101086

Contents lists available at ScienceDirect

Results in Optics

journal homepage: www.elsevier.com/locate/rio

Sum-frequency generation with modified anomalous vortex beams

Bikash K. Das [a,*], Camilo Granados [b], Wenlong Gao [b], Stephan Fritzsche [a,c,d]

[a] Theoretisch-Physikalisches Institut, Friedrich-Schiller-Universität Jena, Max-Wien-Platz 1, Jena, D-07743, Germany
[b] Eastern Institute of Technology, Ningbo, 315200, China
[c] Helmholtz-Institut Jena, Jena, D-07743, Germany
[d] GSI Helmholtzzentrum für Schwerionenforschung, Darmstadt, D-64291, Germany

ARTICLE INFO

Keywords:
Light matter interactions
Sum-frequency generation
Optical vortices
Orbital angular momentum
Anomalous vortex beams

ABSTRACT

Light beams carrying orbital angular momentum (OAM) provide an additional degree of freedom to control and manipulate light-matter interactions across different energy regimes. Precise control over the beam and dark-core sizes, while maintaining a high value of the topological charge (TC) is crucial for their applications in optical tweezing, optical communication, and microscopy. While perfect optical vortices were engineered to feature TC-independent intensity distribution, their generation method typically involves bulky experimental setup. Furthermore, their detection is non-trivial, as they are not propagation eigenmodes and thus do not maintain their perfect vortex structure during propagation. A more sophisticated beam configuration is the modified anomalous vortex (MAV) beam — a novel class of anomalous vortex beam engineered with controlled self-focusing characteristics. MAV beams are typically characterized by their TC, beam order, and a so-called modification parameter. For extremely high beam order and a unity modification parameter, the beam and dark-core sizes of MAV beams remain nearly independent of the TC. Despite such novel beam properties, their role in driving nonlinear optical phenomena remains largely untested. In this work, we investigate the sum-frequency generation driven by MAV beams. For this nonlinear process, we derive an analytical expression for the complex field amplitude of the sum-frequency beam at the waist plane. Furthermore, we study the evolution of the generated sum-frequency beam in free-space. We thoroughly discuss the underlying OAM selection rule, and analyze how different parameters of the input MAV beams, such as their TC, beam order, modification parameter, and wavelength affect the sum-frequency beam. Moreover, we compare both the power of the sum-frequency beam generated by fundamental MAV, traditional AV, and Laguerre–Gaussian vortex beams, as well as the corresponding conversion efficiency of the process.

1. Introduction

Optical vortices, with their ability to carry orbital angular momentum (OAM), have enabled diverse applications, such as particle trapping and manipulation (Kovalev et al., 2016; Ng et al., 2010), optical communication and optical encryption (Shao et al., 2018; Liu et al., 2019; Yang et al., 2022; Yuan et al., 2025; Yang et al., 2026), microscopy and imaging (Wang et al., 2017; Sun et al., 2025; Ma et al., 2026), and quantum entanglement (Fickler et al., 2016; Xu et al., 2025). Generally, vortex beams are characterized by the presence of a helical (or, spiral) phase term $\exp(il\theta)$ in their electric field distribution, where l is called the topological charge (TC, alternatively an OAM of $l\hbar$ per photon with $\hbar = h/2\pi$ being the reduced Planck's constant) and θ represents an azimuthal coordinate (Allen et al., 1992). In essence, the magnitude of the TC determines the number of 2π shifts occurring around the singularity along the beam's azimuth, while its sign indicates the handedness of the helical wavefront. Several optical beams including Laguerre–Gaussian (LG) (Allen et al., 1992; Padgett et al., 1996), Bessel–Gauss (BG) (Xie et al., 2015; Zhao et al., 2019), circular Airy (Zheng et al., 2022), and Lorentz–Gauss vortex beams (Ni and Zhou, 2013; Zhou, 2014) are characterized by their helical wavefronts. However, for conventional vortices, a fundamental challenge is to control the beam and the dark-core sizes without compromising the TC, given that these parameters are intrinsically coupled. This, in turn, restricts their utilization in the efficient trapping of microscopic particles, and multiplexing of vortex modes with high OAMs for high-capacity data transmission in fiber-optic networks.

To remove such constraints, novel "perfect" optical vortices (POVs) were engineered in 2013, which typically display consistent beam characteristics regardless of their TC (Ostrovsky et al., 2013). The generation of POV beams can be accomplished through several techniques, such as the Fourier transformation of BG beams (Vaity and Rusch, 2015), the Fourier transformation of LG beams with high radial

* Corresponding author.
E-mail address: bikash.kumar.das@uni-jena.de (B.K. Das).

https://doi.org/10.1016/j.rio.2026.101086
Received 19 April 2026; Received in revised form 18 June 2026; Accepted 15 July 2026
Available online 20 July 2026
2666-9501/

indices (Guo et al., 2022; Das et al., 2025b), as well as the use of dielectric metasurfaces (Liu et al., 2024; He et al., 2022), transmission liquid crystal spatial light modulators (Anaya Carvajal et al., 2017), and digital micromirror devices (Chen et al., 2015), to name a few. A significant drawback, however, is that these techniques require elaborate optical setups and extremely precise design. On the other hand, modified anomalous vortex (MAV) beams constitute a distinct class of anomalous vortices, characterized by their TC, beam order, and a so-called modification parameter (Al-Ahsab et al., 2024). Under specific circumstances, these beams can exhibit behavior analogous to POVs. For example, in Ref. Al-Ahsab et al. (2024), the authors demonstrated that for higher beam orders and a unity modification parameter, the beam size and ring width of MAV beams remain nearly constant as the TC increases — a key characteristic of "perfect" vortex beams. Like POVs, moreover, MAV beams also exhibit self-focusing properties — a distinct advantage for applications, such as efficient optical data transmission and imaging in turbulent environments. Additionally, a straightforward method for generating these beams is to use a spatial light modulator, which is programmed with a phase hologram containing the beam's complete specifications. While the production of MAV beams using existing digital devices is currently limited to the visible spectral range, it can be readily extended to large wavelength, such as the near-infrared spectral range. However, generating MAV beams at wavelengths significantly shorter than the visible light – extending into the extreme ultraviolet and X-ray ranges – is not feasible with the optical devices being used for visible light generation.

Frequency up-conversion is a fundamental optical process that harnesses nonlinear phenomena inside material media to generate shorter, and often extreme wavelengths of light. Both perturbative and non-perturbative nonlinear processes – including second-harmonic generation (SHG), third-harmonic generation (THG), sum-frequency generation (SFG), and high-order harmonic generation (HHG) – are widely used to generate radiation across the visible-to-extreme ultraviolet spectrum, sometimes to the soft X-ray range as well based on the driving beam parameters (Das et al., 2026). In general, perturbative nonlinear processes describe light-matter interaction under the condition where an applied external field is significantly weaker than the internal atomic fields binding electrons. In this regime, the external field can be treated as a small perturbation to system. Consequently, the induced polarization response is quantitatively modeled as a power series expansion in the strength of the applied external field. In contrast, when the external field strength becomes comparable to the atomic binding strength, the perturbative framework for light-matter interaction fails, and pronounced non-perturbative effects emerge (Das et al., 2026). The generated up-converted beams may or may not carry OAM, depending on whether the driving beam itself possesses a vortex structure. For example, during second- and third-harmonic generation with OAM beams in nonlinear crystals, a linear up-scaling rule for the OAM i.e., $l_q = q \times l$ has been demonstrated, where l_q, and l denote the OAM of the qth order harmonic, and OAM of the driving beam, respectively. This, in turn, establishes the fact that frequency up-converted beams indeed inherit vortex characteristics from driving OAM beams. Furthermore, a detailed analysis of different kinds of phase-matching methods, such as birefringent phase-matching (BPM, a critical phase-matching technique, where the orientation of the crystal optic axis with respect to the driving field's polarization direction is leveraged to achieve perfect or near-perfect phase-matching) and quasi-phase matching (QPM, a non-critical phase-matching technique, where the periodic-poling of certain nonlinear crystals are utilized to achieve perfect or near-perfect phase-matching) for frequency conversion with nonlinear crystals, when OAM beams drive the processes were reported in the past (Dholakia et al., 1996; Shao et al., 2013; Zhou et al., 2014). Similarly, in the SFG process, tuning the wavelength and OAM of the two input beams allows direct and simultaneous control over the wavelength and OAM of the generated SFG beam, in full compliance with the energy and OAM conservation (Li et al., 2015; Qi et al., 2022). In atomic targets, the HHG process driven by OAM beams has not only produced extreme ultraviolet radiations with extremely high and even time-varying OAMs but has also enabled the generation of twisted attosecond pulses (Das et al., 2026; Kong et al., 2017; Gariepy et al., 2014; Rego et al., 2019; de las Heras et al., 2024). Despite their novel physical properties, MAV beams have received little to no attention in the literature – specifically, in the context of driving nonlinear processes in atomic gases and crystals – where research efforts have instead been concentrated more on conventional vortices such as LG and BG beams. Using MAV beams to drive both perturbative and non-perturbative nonlinear processes could enable the generation of such beams at wavelengths shorter than visible light, with tunable OAM. This approach may extend their applicability down to the nanometer scale. Furthermore, for higher beam orders and a unity modification parameter, the beam size of the MAV beam grows at a much slower rate than that of conventional LG beams with the same Gaussian waist and over the same range of TCs. Consequently, employing MAV beams in nonlinear optical processes may enhance both the photon flux and the spatial coherence of the generated radiation, which in turn leads to better focusability.

In this work, we explore sum-frequency generation driven by MAV beams within a periodically-poled potassium titanyl phosphate (PPKTP) crystal. Within the no pump depletion approximation, thin crystal approximation, and assuming ideal phase-matching conditions, we derive an analytical expression describing the complex field amplitude of the generated SFG beam at its waist plane. This result is then extended to finite propagation distances through an ABCD-matrix treatment combined with the Huygens–Fresnel integral, allowing full characterization of the generated beam in terms of its intensity and phase profiles. Additionally, we examine the conservation of OAM in the SFG process. We also analyze how MAV beams with modified TC, beam order, modification parameter, and wavelength affect the intensity and phase distribution of the obtained sum-frequency beam. Moreover, under identical conditions, we compare both the power of the sum-frequency beam generated by input MAV, AV, and LG beams and the corresponding conversion efficiency, in order to demonstrate how MAV beams dominate over AV and LG beams in these respects.

2. Theoretical description of the fundamental MAV beam and modeling of the SFG process

This section begins with an introduction to MAV beams and a discussion on their key physical properties at the generation (or source) plane. We then explore the nonlinear interaction of MAV beams with a PPKTP crystal via the SFG process. Subsequently, we theoretically calculate the SFG power and conversion efficiency of the process and examine how the TC, beam order, modification parameter, and input beam wavelengths influence these properties.

2.1. *Description of the fundamental MAV beam*

The concept of an MAV beam was theoretically proposed and experimentally realized using holographic techniques and customized phase masks in 2024 (Al-Ahsab et al., 2024). Briefly summarizing the experimental setup for generating MAV beams: the output Gaussian beam from a continuous-wave laser first passes through a neutral density filter to control its power. A linear polarizer then adjusts its polarization profile, converting it into a linearly polarized Gaussian beam. This beam illuminates a spatial light modulator loaded with a customized phase mask containing the necessary information for the desired MAV beam, thereby generating the target beam. The phase mask is typically designed using holographic techniques, where the desired output beam (an MAV beam in this case) is interfered with a tilted plane wave.

The complex field amplitude of the MAV beam at the source plane i.e., at $z = 0$, can be written as (Al-Ahsab et al., 2024):

$$E_{MAV}(\hat{r}, \theta) = E_0 \left(\frac{\hat{r}}{w_0} \right)^{2n+|l|} e^{-\frac{\hat{r}^2}{w_0^2}} e^{-il\theta} \tag{1}$$

where we define $\hat{r} = \sqrt{(\delta n+1)}r$, and ($r = \sqrt{x^2+y^2}, \theta = \arctan(y/x)$) are the polar coordinates of the beam at the source plane. In Eq. (1), $E_0 = \sqrt{\frac{2^{2n+|l|+1}(\delta n+1)P_0}{\pi c\epsilon_0 s w_0^2 (2n+|l|)!}}$, w_0, P_0, n, l, δ denote a constant amplitude, beam waist size, input power, beam order, topological charge (TC), and modification parameter of the MAV beam, respectively. Additionally, $c \approx 3\times10^8$ m/s is the speed of light in vacuum, $\epsilon_0 \approx 8.854\times10^{-12}$ F/m is the vacuum permittivity, and $s(=1)$ is the refractive index of the MAV beam at a given wavelength λ in vacuum. Moreover, the beam order n can take either zero or non-zero positive integer values only. For a vanishing beam order ($n = 0$) and a vanishing modification parameter ($\delta = 0$), Eq. (1) basically represents an LG_0^l mode. However, for a non-vanishing beam order ($n \neq 0$) and a vanishing TC ($l = 0$), Eq. (1) represents hollow Gaussian beams. It is interesting to highlight that for $\delta = 0$, Eq. (1) reduces to the complex field amplitude of the traditional anomalous vortex (AV) beam (Al-Ahsab et al., 2024). Experimentally, MAV beams with a beam order as high as $n = 10$ have been generated using a spatial light modulator. Extending this beam order to even higher values is straightforward, as it only requires customizing the phase mask with the desired beam order information for a given modification parameter and TC. The value of the modification parameter δ typically ranges from 0 to 1 (Al-Ahsab et al., 2024). It should be noted that negative values of δ would yield imaginary values for both the beam size and the radius of the maximum intensity ring, which are physically meaningless. Hence, we restrict δ to non-negative values less than or equal to unity. Basically, the modification parameter adjusts the self-focusing characteristics of MAV beams while retaining the fundamental properties of traditional anomalous vortex beams. Furthermore, the modification parameter allows for exact tuning of the self-focusing point. This enhanced precision in governing the self-focusing properties not only refines beam control but also boosts the versatility of MAV beams across numerous scientific and technological domains. It is important to note that like POVs, MAV beams also display self-focusing characteristics, when they propagate in free-space and different material media (Das et al., 2024; Al-Ahsab et al., 2024). By self-focusing, we mean to say that the profile size of these beams attain a minimum value accompanied by a sharp enhancement in their beam intensity during the course of propagation, without the involvement of any nonlinear optical effects (such as the Kerr effect for high intensity laser beams) or external focusing optics.

Fig. 1 displays the transverse intensity and phase distributions of the MAV beam for different values of the TC ($l = 1, 2, 5$), while the beam order and modification parameter values are kept fixed i.e., $n = 1$ and $\delta = 1$. It can be seen from Fig. 1(a), (c), and (e) that the beam size, as well as the dark-core size expands monotonically with increasing TC values. This behavior of the MAV beam is analogous to what we typically see in case of conventional vortices such as LG and BG beams. We can quantitatively understand how the size of the MAV beam increases with the TC, if the beam width is computed by means of the second-moment of intensity definition, as shown in Ref. Das et al. (2025a): $w_{MAV}(l) = w_0\sqrt{\frac{2n+|l|+1}{\delta n+1}}$. This relation between the beam size and the order as well as the TC of the beam shows that $w_{MAV}(l) \propto \sqrt{|l|}$, for a fixed value of n and δ. Therefore, an increase in the value of l leads to an enhancement in the beam size. Furthermore, from Fig. 1(a), (c), and (e), it can be observed that the radius of the maximum intensity ring of the MAV beam increases with increasing TC values. To understand such behavior, we calculate the radius of the maximum intensity ring, r_{max}^{MAV}, using the definition $\frac{\partial |E_{MAV}(r,\theta)|^2}{\partial r} = 0$, which results in: $r_{max}^{MAV} = w_0\sqrt{\frac{2n+|l|}{2(\delta n+1)}}$. This relationship clearly depicts that $r_{max}^{MAV} \propto \sqrt{|l|}$. As shown in the expression above, for a given beam waist, TC, and beam order, the radius of the maximum intensity ring varies inversely with the modification parameter. Additionally, by counting the number of 2π shifts along the azimuthal coordinate of the MAV beam in the transverse plane as shown in Fig. 1(b), (d), and (f), it is possible to extract the TC carried by the beam, which are $l = 1, 2, 5$, respectively.

Furthermore, we increase the value of the beam order to $n = 10$ and plot the intensity and phase distributions of the MAV beam for a unity modification parameter, and for different TCs ($l = 1, 2, 5$). The results are presented in Fig. 2. It can be seen from Fig. 2(a), (c), and (e) that as the TC increases, the beam size, dark-core size, and the radius of the maximum intensity ring of MAV beams also increase. However, the rate of this enhancement is much smaller compared to that observed for MAV beams with a low beam order (e.g., for $n = 1$ in Fig. 1(a), (c), and (e)). It is expected that the rate of this enhancement would diminish even further if MAV beams with $n > 10$ are employed. A comparison between Figs. 1 and 2 reveals the following: (1) For $l = 1$ and $\delta = 1$, the TC-dependent beam width is precisely the same for the MAV beam with $n = 1$ and $n = 10$ i.e., $w_{MAV}(l = 1, n = 1) = w_{MAV}(l = 1, n = 10) = 20\sqrt{2}$ μm, for $w_0 = 20$ μm. However, the ring width of the MAV beam decreases upon increasing the value of n. (2) For MAV beams with $l > 1$, the TC-dependent beam size is higher for lower values of n. Therefore, the effect of increasing the beam order values of MAV beams is to mitigate the growth of the beam size with increasing l values. Similar to Fig. 1, the TC information of the beam can be extracted by counting the number of 2π phase shifts along the beam's azimuth, as shown in Fig. 2(b), (d), and (f).

In Fig. 3(a), we show the TC-dependent beam width of MAV beams for different values of n i.e., $n = 1$ (as blue dots), and $n = 10$ (as red dots). It can be clearly seen from the figure that in both the cases, the beam width expands with increasing l values. However, this growth is very slow for MAV beams with $n = 10$, when compared to MAV beams with $n = 1$. For even higher values of n, we expect that the beam width will display a near-flat line i.e., it becomes nearly independent of the TCs. Such a feature is analogous to what we typically see in POV beam's intensity distribution. It is important to note that in case of perfect vortex beams, the beam width remains nearly independent of the TC, when the ratio of the ring radius (R) to the half-ring width (w_p) of the beam attains extremely higher values. Therefore, the role played by n in case of MAV beams is analogous to that of the ratio R/w_p in case of perfect vortex beams. Furthermore, to better understand the role of the modification parameter, δ, in controlling the beam size of the MAV beam, we compare the TC-dependent beam width of MAV beams with that of conventional LG beams (see Fig. 3(a) and (b)). Here, it is important to note that the TC-dependent beam width of LG beams can be expressed as (following the second-moment of intensity definition): $w_{LG}(l) = w_0\sqrt{2p+|l|+1}$, where p is called the radial index (or, the radial quantum number) and it is quantitatively connected to the number of off-axis rings in the transverse intensity distribution of LG beams. It is interesting to note that the TC-dependent beam widths of MAV and LG beams become identical i.e., $w_{MAV}(l) = w_{LG}(l) = \sqrt{|l|}$, when $\delta = 0, n = 0$, and $p = 0$. This clearly shows that there is some hidden relationship between n and δ values of MAV beams, and p values of LG beams. For a better comparison of the TC-dependent beam widths, we fix the beam waist w_0 to 20 μm for both MAV and LG beams. It can be clearly seen from Fig. 3 that the beam width of MAV beams is always less than that of their LG counterparts. So, it is the modification parameter which is solely responsible for the reduced beam size of MAV beams, when compared with LG beams of identical TCs. We strongly believe that the novel features exhibited by MAV beams can potentially provide significant advantages over conventional LG beams in applications, such as optical trapping, optical communication, stimulated emission depletion microscopy, and nonlinear optics.

2.2. Description of the SFG process driven by MAV beams

SFG is a nonlinear optical phenomenon governed by the second-order nonlinear susceptibility tensor, where two laser beams with different frequencies, when simultaneously irradiate a nonlinear crystal, produce a coherent light beam whose frequency corresponds to the sum of frequencies of the input light beams. In order to investigate the SFG process in QPM crystals (a PPKTP crystal in this case), the

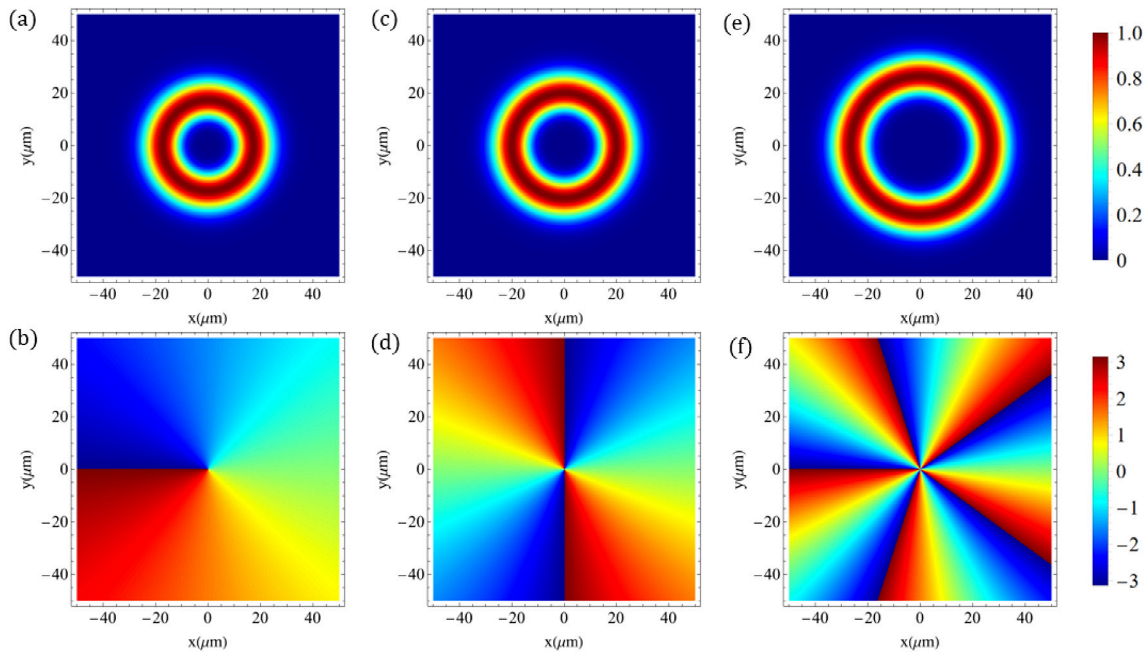

Fig. 1. Transverse intensity and phase distributions of MAV beams at the source plane. (a)–(b) $l = 1, n = 1, \delta = 1$, (c)–(d) $l = 2, n = 1, \delta = 1$, and (e)–(f) $l = 5, n = 1, \delta = 1$. The intensity colorbar is normalized to the respective maximum value for each panel. The figure shows that for a low beam order and a modification parameter equal to one, both the beam size and the radius of the maximum intensity ring of MAV beams increase monotonically with the TC.

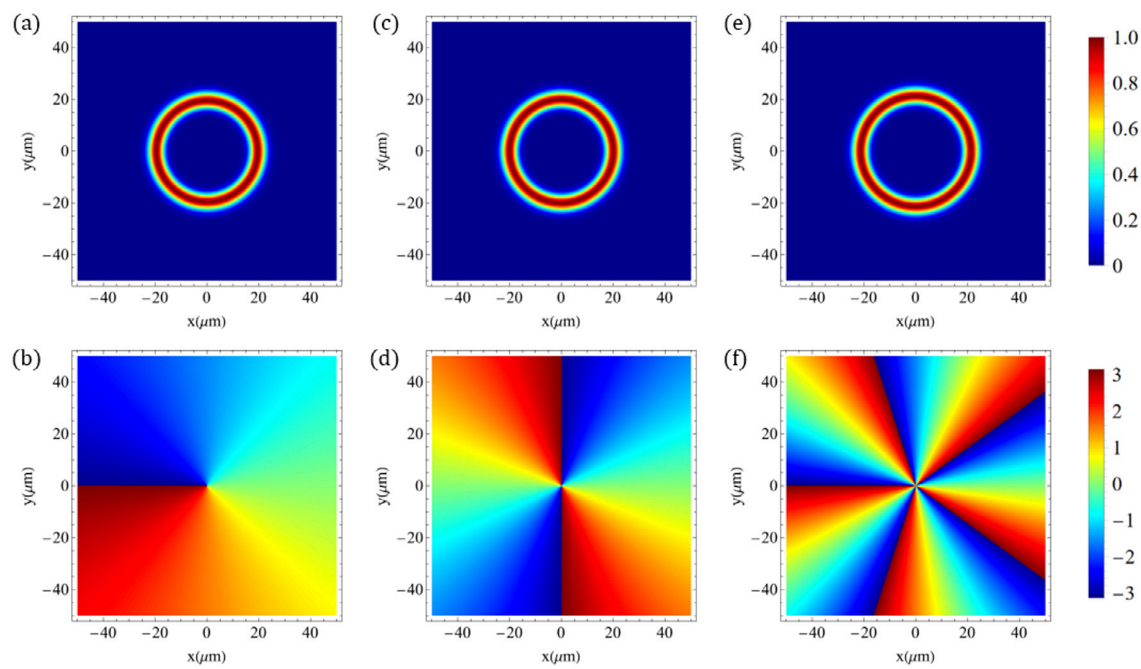

Fig. 2. Transverse intensity and phase distributions of MAV beams at the source plane. (a)–(b) $l = 1, n = 10, \delta = 1$, (c)–(d) $l = 2, n = 10, \delta = 1$, and (e)–(f) $l = 5, n = 10, \delta = 1$. The intensity colorbar is normalized to the respective maximum value for each panel. The figure shows that for a higher beam order and a modification parameter equal to one, both the beam size and the radius of the maximum intensity ring of MAV beams increase at a much slower rate compared to those with a low beam order, as illustrated in Fig. 1.

following coupled nonlinear wave equations are used to describe the interaction between the MAV waves (Li et al., 2015):

$$\begin{aligned}\frac{dE_{1pol}(z)}{dz} &= iK_1 E^*_{2pol} E_{3pol} e^{-i\Delta kz}\\ \frac{dE_{2pol}(z)}{dz} &= iK_2 E^*_{1pol} E_{3pol} e^{-i\Delta kz}\\ \frac{dE_{3pol}(z)}{dz} &= iK_3 E_{1pol} E_{2pol} e^{i\Delta kz},\end{aligned} \tag{2}$$

where $E_{jpol}(z) = E_{MAV}(r', \theta', z)$ with $j = 1, 2, 3$ represents the amplitudes of the three interacting waves involved in the process, 'pol' stands for their polarization (either ordinary or extraordinary), '$*$' denotes the complex conjugate, and $E_{MAV}(r', \theta', z)$ is the complex field amplitude of the MAV beam at some propagation distance z, which can easily be obtained by substituting Eq. (1) in the Huygens–Fresnel integral (Al-Ahsab et al., 2024). Furthermore, $\Delta k = k_{3pol} - k_{1pol} - k_{2pol} - G$ is the phase-mismatch factor (which typically controls the coherence length

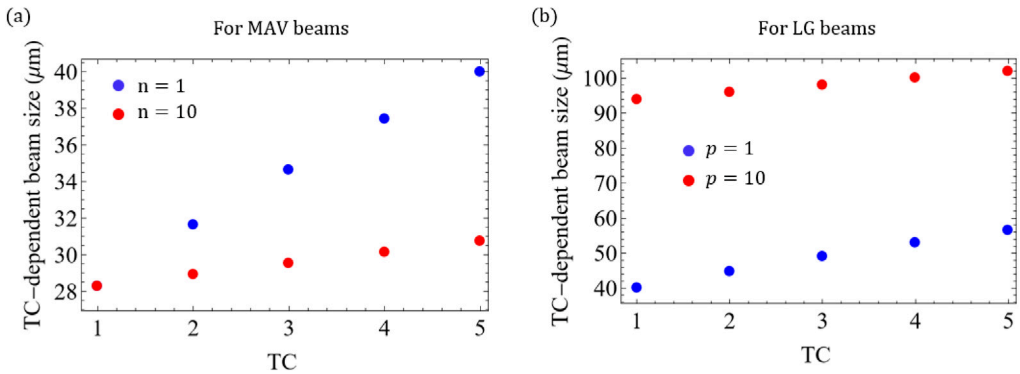

Fig. 3. TC-dependent beam width for MAV beams in (a), and LG beams in (b). Here, we use the following beam parameters: w_0 = 20 μm, δ = 1. The beam width of MAV beams increases more slowly with an increase in the TC for a higher beam order (n = 10) than for a lower beam order (n = 1). Likewise, for LG beams, increasing the radial index reduces the growth rate of the beam width as the TC increases. For identical values of waist size, TC, radial index p, beam order n, and for a unity modification parameter, the beam width of LG beams is always greater than that of MAV beams.

in the interaction, L_{coh}, through the relation: $L_{coh} = \pi/\Delta k$), where $k_{3pol}, k_{2pol}, k_{1pol}$ denote the wave vectors associated with the three interacting MAV waves and G is the phase-mismatch contribution coming from the QPM crystal. The coefficient, $K_j = \frac{2\Omega_j d_{33}}{\pi s_j c}$, where Ω_j represents the angular frequencies of the interacting MAV waves, s_j denotes their refractive indices in the QPM crystal, and d_{33} is the effective nonlinear coefficient of the PPKTP crystal which quantifies the strength of the nonlinear interaction and is mathematically connected to the nonlinear susceptibility. In general, PPKTP is a ferroelectric nonlinear crystal with a unique structure that facilitates efficient frequency conversion through QPM. The crystal consists of alternating domains with oppositely oriented spontaneous polarizations, which enables QPM to correct the phase-mismatch in the nonlinear interactions (SFG process in this case). Additionally, this crystal shows transparency for a wide range of wavelengths (typically between 0.4–3 μm), possesses large effective nonlinear coefficient (d_{33} = 16.9 pm/V), and exhibits high optical damage threshold. Our theoretical treatment operates under the assumption of negligible pump depletion, whereby the intensity of the input MAV beams is considered invariant as they propagate through the QPM crystal, allowing us to isolate the dynamics of the generated SFG field. Additionally, in the case of weak interaction efficiency of frequency mixing processes, depletion of pump beams can also be neglected (Beržanskis et al., 1998). Additionally, because the Rayleigh ranges of the input MAV beams – approximately 1621 μm for the 775 nm beam and 810 μm for the 1550 nm beam, assuming an identical waist size of 20 μm for both – are significantly larger than the length of the nonlinear crystal (200 μm in this case), we neglect diffraction effects arising from the finite beam size and adopt the thin crystal approximation. If we assume that the perfect phase-matching condition i.e., $\Delta k = 0$, is satisfied during the course of the interaction which is relatively easier to achieve with thin nonlinear crystals (Zhang et al., 2023), then we can write the complex field amplitude of the SFG beam at the waist plane as follows:

$$\begin{aligned}
E_{SFG}(r,\theta) &= iK_3 E_{1pol} E_{2pol} \int_0^L e^{i\Delta k z} dz \\
&= iK_3 E_{1pol} E_{2pol} L \\
&= \frac{2id_{33}\Omega_3 L}{\pi s_3 c} E_{0,1} E_{0,2} \left(\frac{\hat{r}_1}{w_{0,1}}\right)^{2n_1+|l_1|} e^{-\frac{\hat{r}_1^2}{w_{0,1}^2}} e^{-il_1\theta} \left(\frac{\hat{r}_2}{w_{0,2}}\right)^{2n_2+|l_2|} \\
&\times e^{-\frac{\hat{r}_2^2}{w_{0,2}^2}} e^{-il_2\theta}
\end{aligned} \tag{3}$$

where L denotes the length of the PPKTP crystal and $\hat{r}_i = \sqrt{\delta_i n_i + 1}r$ ($i = 1,2$). Here, $E_{0,1} = \sqrt{\frac{2^{2n_1+|l_1|+1}(\delta_1 n_1+1)P_{0,1}}{\pi c\epsilon_0 s_1 w_{0,1}^2 (2n_1+|l_1|)!}}$ and $E_{0,2} = \sqrt{\frac{2^{2n_2+|l_2|+1}(\delta_2 n_2+1)P_{0,2}}{\pi c\epsilon_0 s_2 w_{0,2}^2 (2n_2+|l_2|)!}}$ are the peak field amplitudes of the MAV beams used for the SFG process. Similarly, $(P_{0,1}, P_{0,2})$, and $(w_{0,1}, w_{0,2})$ are the powers, and beam waist sizes of the input MAV beams, respectively. Additionally, (l_1, l_2), (n_1, n_2), (δ_1, δ_2), and (s_1, s_2) represent the TCs, beam orders, modification parameters, and refractive indices of the input MAV beams, respectively. Note that we introduce different refractive indices (s_1, s_2) into the peak field amplitudes of MAV beams ($E_{0,1}$, $E_{0,2}$), since they possess different wavelengths and are interacting in a physical medium (a PPKTP crystal in our study). It is also important to note that while deriving Eq. (3) from Eq. (2), we remove the z-dependence from both the input MAV beams and the SFG output. This is justified in the tight-focusing approximation because the main contribution to the SFG output comes from the beam spot i.e., at the waist plane where the beam intensity is maximum. It is worth noting that the various approximations employed in this model have already been adopted in the theoretical description of the SFG process driven by LG beams, and the corresponding theoretical findings are in good agreement with experimental results (Li et al., 2015). If a non-zero phase-mismatch factor ($\Delta k \neq 0$) is taken into account for this SFG interaction, it can easily be expected that the intensity distribution of the sum-frequency beam and the conversion efficiency of the process will be hampered.

We can rewrite Eq. (3) in a more simplified form as follows:

$$E_{SFG}(r,\theta) = E_{0,3} r^{\mu} e^{-\alpha r^2} e^{-il_{SFG}\theta} \tag{4}$$

with

$$\begin{aligned}
E_{0,3} &= \frac{2id_{33}\Omega_3 L}{\pi s_3 c} E_{0,1} E_{0,2} \left(\frac{\sqrt{\delta_1 n_1 + 1}}{w_{0,1}}\right)^{2n_1+|l_1|} \left(\frac{\sqrt{\delta_2 n_2 + 1}}{w_{0,2}}\right)^{2n_2+|l_2|} \\
\mu &= 2n_1 + 2n_2 + |l_1| + |l_2| \\
l_{SFG} &= l_1 + l_2 \\
\alpha &= \frac{(\delta_1 n_1 + 1)}{w_{0,1}^2} + \frac{(\delta_2 n_2 + 1)}{w_{0,2}^2}.
\end{aligned} \tag{5}$$

Eq. (4) basically defines the complex field amplitude of the SFG beam at its waist, which coincides with the generation plane. In a typical experimental setup, however, the detector is positioned downstream from the nonlinear crystal. Consequently, the theoretical model must be extended to incorporate the effects of free-space propagation of the SFG beam. Within the framework of the paraxial approximation, the propagation of the generated SFG beam can be modeled by using the ABCD matrix formalism and the Huygens–Fresnel integral (Li et al., 2015):

$$\tilde{E}_{SFG}(r',\theta',z) = \frac{i}{\lambda_3 B} e^{-ik_3 z} \int_0^{\infty} r dr \int_0^{2\pi}$$

$$E_{SFG}(r,\theta)e^{-\frac{ik_3}{2B}(Ar^2-2rr'\cos(\theta'-\theta)+Dr'^2)}d\theta \tag{6}$$

where (r',θ') are the beam coordinates at some propagation distance z and $k_3=\frac{2\pi}{\lambda_3}$ is the magnitude of the wave vector of the SFG beam with $\lambda_3=\frac{\lambda_1\lambda_2}{\lambda_1+\lambda_2}$ representing the wavelength of the SFG beam, λ_1 and λ_2 are the wavelengths of the input MAV beams. A, B, C, and D are elements of the transfer matrix, which represents a physical optical system. If we substitute Eq. (4) into Eq. (6) and solve the angular integral by using the Bessel function of the first kind, we obtain:

$$\begin{aligned}\tilde{E}_{SFG}(r',\theta',z) &= 2\pi(-i)^{l_{SFG}}\frac{iE_{0,3}}{\lambda_3 B}e^{-ik_3 z}e^{-\frac{ik_3Dr'^2}{2B}}e^{-il_{SFG}\theta'}\\ &\times\int_0^\infty r^\mu e^{-\left(\alpha+\frac{ik_3A}{2B}\right)r^2}J_{l_{SFG}}\left(\frac{k_3rr'}{B}\right)rdr.\end{aligned} \tag{7}$$

To solve the radial integral in Eq. (7), we use the following identity (Gradshteyn and Ryzhik, 2007):

$$\int_0^\infty x^q e^{-ax^2}J_u(bx)dx=\frac{b^u\Gamma\left(\frac{q+u+1}{2}\right)}{2^{u+1}a^{\frac{q+u+1}{2}}\Gamma(u+1)}\,{}_1F_1\left[\frac{q+u+1}{2};u+1;-\frac{b^2}{4a}\right] \tag{8}$$

with Re$(a)>0$, Re$(q+u)>-1$. We can use Eq. (8) to solve the radial integral in Eq. (7) and to obtain:

$$\begin{aligned}\tilde{E}_{SFG}(r',\theta',z) &= 2\pi(-i)^{l_{SFG}}\frac{iE_{0,3}}{\lambda_3 B}e^{-ik_3 z}e^{-\frac{ik_3Dr'^2}{2B}}e^{-il_{SFG}\theta'}\\ &\times\frac{\Gamma\left(\frac{l_{SFG}}{2}+\frac{\mu+1}{2}+\frac{1}{2}\right)}{\Gamma(l_{SFG}+1)}\\ &\times\frac{\left(\frac{k_3r'}{B}\right)^{l_{SFG}}}{2^{l_{SFG}+1}\left(\alpha+\frac{ik_3A}{2B}\right)^{\frac{l_{SFG}+\mu+2}{2}}}\\ &\times\,{}_1F_1\left[\frac{l_{SFG}+\mu+2}{2};l_{SFG}+1;-\frac{\left(\frac{k_3r'}{B}\right)^2}{4\left(\alpha+\frac{ik_3A}{2B}\right)}\right]\end{aligned} \tag{9}$$

Since we propagate the SFG beam in free-space for a distance z after its generation in the waist plane (i.e., $z=0$), the ABCD transfer matrix can be written as:

$$\begin{pmatrix}A & B\\ C & D\end{pmatrix}=\begin{pmatrix}1 & z\\ 0 & 1\end{pmatrix} \tag{10}$$

After substituting Eq. (10) into Eq. (9), we obtain:

$$\begin{aligned}\tilde{E}_{SFG}(r',\theta',z) &= 2\pi(-i)^{l_{SFG}}\frac{iE_{0,3}}{\lambda_3 z}e^{-ik_3 z}e^{-\frac{ik_3r'^2}{2z}}e^{-il_{SFG}\theta'}\\ &\times\frac{\Gamma\left(\frac{l_{SFG}}{2}+\frac{\mu+1}{2}+\frac{1}{2}\right)}{\Gamma(l_{SFG}+1)}\\ &\times\frac{\left(\frac{k_3r'}{z}\right)^{l_{SFG}}}{2^{l_{SFG}+1}\left(\alpha+\frac{ik_3}{2z}\right)^{\frac{l_{SFG}+\mu+2}{2}}}\\ &\times\,{}_1F_1\left[\frac{l_{SFG}+\mu+2}{2};l_{SFG}+1;-\frac{\left(\frac{k_3r'}{z}\right)^2}{4\left(\alpha+\frac{ik_3}{2z}\right)}\right]\end{aligned} \tag{11}$$

where $1F1[..;..;..]$ is the Confluent Hypergeometric function and $\Gamma(...)$ is the Euler-Gamma function. Eq. (11) is central to our analysis, which readily confirms the OAM selection rule in the SFG process: $l_{SFG}=l_1+l_2$, where l_{SFG}, l_1, and l_2 represent the OAM of the SFG beam, and two input MAV beams, respectively. If we substitute the expressions for $E_{0,3},\mu,l_{SFG}$, and α from Eq. (5) into Eq. (11), we obtain the following expression for the complex field amplitude of the SFG beam at a distance z:

$$\begin{aligned}\tilde{E}_{SFG}(r',\theta',z) &= 2\pi(-i)^{l_1+l_2}\\ &\times\left(\frac{i*\frac{2id_{33}\Omega_3L}{\pi s_3c}E_{0,1}E_{0,2}\left(\frac{\sqrt{\delta_1n_1+1}}{w_{0,1}}\right)^{2n_1+|l_1|}\left(\frac{\sqrt{\delta_2n_2+1}}{w_{0,2}}\right)^{2n_2+|l_2|}}{\lambda_3 z}\right)\\ &\times\frac{\left(\frac{k_3r'}{z}\right)^{l_1+l_2}\Gamma(\beta)}{2^{l_1+l_2+1}\left(\frac{(\delta_1n_1+1)}{w_{0,1}^2}+\frac{(\delta_2n_2+1)}{w_{0,2}^2}+\frac{ik_3}{2z}\right)^\beta\Gamma(l_1+l_2+1)}\\ &\times\,{}_1F_1\left[\beta;l_1+l_2+1;-\frac{\left(\frac{k_3r'}{z}\right)^2}{4\left(\frac{(\delta_1n_1+1)}{w_{0,1}^2}+\frac{(\delta_2n_2+1)}{w_{0,2}^2}+\frac{ik_3}{2z}\right)}\right]\\ &\times e^{-ik_3z}e^{-\frac{ik_3r'^2}{2z}}e^{-i(l_1+l_2)\theta'}\end{aligned} \tag{12}$$

where $\beta=\frac{l_1+l_2+2n_1+2n_2+|l_1|+|l_2|+2}{2}$. With these results, we can express the intensity $(\tilde{I}_{SFG}(r',z))$ and phase $(\tilde{\Phi}_{SFG}(r',\theta',z))$ of the SFG beam as:

$$\begin{aligned}\tilde{I}_{SFG}(r',z) &= |\tilde{E}_{SFG}(r',\theta',z)|^2\\ \tilde{\Phi}_{SFG}(r',\theta',z) &= Arg[\tilde{E}_{SFG}(r',\theta',z)]\end{aligned} \tag{13}$$

where $Arg[v]$ denotes the argument of a complex number v. Basically, we have used Eqs. (12) and (13) to plot the intensity and phase distributions of the SFG beam under different conditions, as will be shown in the next section.

2.3. Power of the SFG beam

The power of the SFG beam is a macroscopic measure of the rate at which photon energy at the new, higher frequency is radiated from the nonlinear interaction region. It directly reflects the efficiency with which the nonlinear crystal converts the combined power of the two input beams into this coherent up-converted light. Here, we compute the power of the SFG beam at the waist plane as follows (Das et al., 2025e):

$$P_{SFG}=4\pi s_3c\epsilon_0\int_0^\infty|E_{SFG}(r,\theta)|^2rdr \tag{14}$$

By Substituting Eq. (4) into Eq. (14), we obtain:

$$P_{SFG}=4\pi s_3c\epsilon_0|E_{0,3}|^2\int_0^\infty r^{2\mu+1}e^{-2\alpha r^2}dr \tag{15}$$

The radial integral in Eq. (15) is basically a Gaussian integral, which can easily be solved using the Euler-Gamma function: $\Gamma(p)=\int_0^\infty e^{-t}t^{p-1}dt$. The radial integral $\int_0^\infty r^{2\mu+1}e^{-2\alpha r^2}dr$ evaluates to $\Gamma(\mu+1)/2(2\alpha)^{\mu+1}$. Therefore, the power of the SFG beam is evaluated to:

$$P_{SFG}=\frac{2\pi s_3c\epsilon_0|E_{0,3}|^2\Gamma(\mu+1)}{(2\alpha)^{\mu+1}} \tag{16}$$

The expressions for $E_{0,3},\alpha$, and μ from Eq. (5) can be substituted into Eq. (16) to analyze how various parameters, such as the TC, beam order, beam waist size of the input MAV beams influence the power of the SFG beam. Now, Eq. (16) can be rewritten as:

$$\begin{aligned}P_{SFG} &= \frac{128d_{33}^2L^2P_{0,1}P_{0,2}}{\pi c\epsilon_0s_3s_1s_2\lambda_3^2w_{0,1}^2w_{0,2}^2}\frac{2^{2n_1+2n_2+|l_1|+|l_2|}(\delta_1n_1+1)(\delta_2n_2+1)}{(2n_1+|l_1|)!(2n_2+|l_2|)!}\\ &\times\left(\frac{(\delta_1n_1+1)}{w_{0,1}^2}\right)^{2n_1+|l_1|}\left(\frac{(\delta_2n_2+1)}{w_{0,2}^2}\right)^{2n_2+|l_2|}\\ &\times\frac{\Gamma(2n_1+2n_2+|l_1|+|l_2|+1)}{\left(\frac{2(\delta_1n_1+1)}{w_{0,1}^2}+\frac{2(\delta_2n_2+1)}{w_{0,2}^2}\right)^{2n_1+2n_2+|l_1|+|l_2|+1}}\end{aligned} \tag{17}$$

Eq. (17) clearly demonstrates that the SFG beam's power holds a direct relationship with the product of input MAV beams' power, square of the crystal length, and square of the effective nonlinear coefficient, whereas it holds an inverse relationship with square of the SFG wavelength and square of the input MAV beams' waist sizes. In contrast to these direct proportionalities, the SFG beam's power depends in a more sophisticated manner on the TC, beam order, and modification parameter of input MAV beams.

2.4. Efficiency of the SFG process

The conversion efficiency, η, of the SFG process is defined as the ratio of the power of the SFG beam to the product of input MAV beams' power i.e.,

$$\eta = \frac{P_{SFG}}{P_{0,1}\times P_{0,2}} = \frac{128 d_{33}^2 L^2}{\pi c\epsilon_0 s_3 s_1 s_2 \lambda_3^2 w_{0,1}^2 w_{0,2}^2} \times \frac{2^{2n_1+2n_2+|l_1|+|l_2|}(\delta_1 n_1+1)(\delta_2 n_2+1)}{(2n_1+|l_1|)!(2n_2+|l_2|)!} \times \left(\frac{(\delta_1 n_1+1)}{w_{0,1}^2}\right)^{2n_1+|l_1|}\left(\frac{(\delta_2 n_2+1)}{w_{0,2}^2}\right)^{2n_2+|l_2|} \times \frac{\Gamma(2n_1+2n_2+|l_1|+|l_2|+1)}{\left(\frac{2(\delta_1 n_1+1)}{w_{0,1}^2}+\frac{2(\delta_2 n_2+1)}{w_{0,2}^2}\right)^{2n_1+2n_2+|l_1|+|l_2|+1}} \tag{18}$$

From Eq. (18), the conversion efficiency of the SFG process is shown to be governed by the interplay of several beam parameters. For example, from Eq. (18), it can be found that the conversion efficiency scales quadratically with the nonlinear crystal length and inversely with the square of the SFG wavelength and the input MAV beams' waist sizes. To evaluate the influence of the TC and beam order on the conversion efficiency, however, it is necessary to fix these parameters for one input beam while varying those of the other.

3. Results and discussion

Let us next discuss how the intensity and phase distributions of the SFG beam is affected by the parameters of the input MAV beams. In particular, we shall consider the SFG beam at different finite positions beyond the waist plane $z = 0$. In our theoretical analysis, we fix the following beam parameters: $P_{0,1} = 15$ W, $P_{0,2} = 15$ W, $s_3 = 1.892$, $L = 200$ μm, $d_{33} = 16.9$ pm/V, $w_{0,1} = 20$ μm, $w_{0,2} = 20$ μm. For simplicity, we fix the values of s_1 and s_2 to unity, although the actual values of s_1 and s_2 could slightly be off from their unity value since the input MAV beams are interacting within a nonlinear crystal. However, small changes in s_1 and s_2 do not alter the quality of the overall results. More specifically, we discuss six different cases in this section: (1) $l_1 = l_2$, $n_1 = n_2$ (small), $\delta_1 = \delta_2$, (2) $l_1 \neq l_2$, $n_1 = n_2$ (small), $\delta_1 = \delta_2$, (3) $l_1 = l_2$, $n_1 = n_2$ (large), $\delta_1 = \delta_2$, (4) $l_1 = l_2$, $n_1 \neq n_2$ (large), $\delta_1 = \delta_2$, and (5) $l_1 = l_2$, $n_1 = n_2$ (small), $\delta_1 \neq \delta_2$. From Case 1 to Case 5, we use $\lambda_1 = 775$ nm, $\lambda_2 = 1550$ nm, and $\lambda_3 = \frac{\lambda_1\lambda_2}{\lambda_1+\lambda_2} = 516.6$ nm. Subsequently, in Case 6, we investigate the influence of the input MAV beams' wavelength on the intensity and phase distributions of the SFG beam. To this end, we employ the same beam and medium parameters as in Case 1, except for the wavelengths, which are set to $\lambda_1 = 1054$ nm, $\lambda_2 = 2000$ nm, and $\lambda_3 = \frac{\lambda_1\lambda_2}{\lambda_1+\lambda_2} = 690.2$ nm. The exact values of $l_1, l_2, n_1, n_2, \delta_1$, and δ_2 are mentioned in each of the cases discussed below.

3.1. Case 1: $l_1 = l_2$, $n_1 = n_2$ (small), $\delta_1 = \delta_2$

In this case, we consider identical values of the TC ($l_1 = l_2$), beam order ($n_1 = n_2$), and modification parameter ($\delta_1 = \delta_2$) for the input MAV beams. However, we limit the beam order to a small value. If we use the conditions $l_1 = l_2 = l$, $n_1 = n_2 = n$, $\delta_1 = \delta_2 = \delta$, $P_{0,1} = P_{0,2} = P_0$, and $w_{0,1} = w_{0,2} = w_0$, the complex field amplitude of the SFG beam at the waist plane can be written as (by using Eq. (4)):

$$E_{SFG}(r,\theta) = \frac{2id_{33}\Omega_3 L}{\pi s_3 c}\frac{2^{2n+|l|+1}(\delta n+1)P_0}{\pi c\epsilon_0\sqrt{s_1 s_2}w_0^2(2n+|l|)!} \times \left(\frac{\sqrt{(\delta n+1)}r}{w_0}\right)^{2(2n+|l|)} \mathrm{e}^{-2\frac{(\delta n+1)r^2}{w_0^2}}\,\mathrm{e}^{-i2l\theta} \tag{19}$$

Eq. (19) represents the second-harmonic of the fundamental MAV beam given in Eq. (1), when $\lambda_3 = \lambda_1/2 = \lambda_2/2$. This result is not surprising since SHG is a special case of SFG, where both the input photons are identical in all aspects and they annihilate to generate a single photon of frequency twice the frequency of the either input. It is interesting to highlight that for $n = 0 = \delta$ and $\lambda_3 = \lambda_1/2 = \lambda_2/2$, Eq. (19) reduces to the second-harmonic field of LG vortex beams, as presented in Ref. Das et al. (2025e). Similarly, for $n \neq 0$, $\delta = 0$, and $\lambda_3 = \lambda_1/2 = \lambda_2/2$, Eq. (19) reduces to the second-harmonic field of traditional AV beams.

In Fig. 4, we show the transverse intensity and phase distributions of the SFG beam at the distance $z = 5000$ μm for two different values of the TCs of the input MAV beams i.e., $l_1 = l_2 = l = 1$ in (a)–(b), and $l_1 = l_2 = l = 2$ in (c)–(d). For this analysis, we fix the values of the beam order and modification parameter to $n_1 = n_2 = n = 1$ and $\delta_1 = \delta_2 = \delta = 1$. From Fig. 4(a), one can clearly see that the SFG beam exhibits vortex characteristics i.e., an intensity null is located at the beam center and there is an azimuthal distribution of energy around the vortex core. This is not surprising since there is a helical phase term, $\exp(-i2l\theta)$, present in Eq. (19). If we insert Eq. (19) into Eq. (6) to understand the propagation dynamics of the SFG beam in free-space, the propagated SFG field, $E_{SFG}(r',\theta',z)$ must accommodate the helical phase term, $\exp(i2l\theta')$, within its field distribution. This, in turn, leads to the vortex characteristics of the SFG beam at finite propagation distances. In addition to the maximum intensity ring surrounding the central dark-core, there also exists a less intense off-axis ring (see Fig. 4(a)). From here on, we call these less intense off-axis rings as "secondary off-axis rings". It is interesting to note that the fundamental MAV beam typically displays a single-bright ring in its intensity distribution for $l = 1$, $n = 1$, and $\delta = 1$ (see Fig. 1(a)) and maintain this single-ring intensity distribution throughout the free-space propagation (Al-Ahsab et al., 2024), which is quite different from what we observe in case of the SFG beam for the same set of input MAV beam parameters i.e., $l_1 = 1 = l_2$, $n_1 = 1 = n_2$, and $\delta_1 = 1 = \delta_2$. It is the nonlinear process itself i.e., the sum-frequency mixing in this case, which imprints such characteristic on to the frequency up-converted SFG beam. As the TC of the input MAV beams increases from $l = 1$ to $l = 2$, the central dark-core and beam sizes of the SFG beam expands (see Fig. 4(a) and (c)). The expansion of the SFG beam size with increasing TC values of the input MAV beams can easily be understood, if we compute the TC-dependent beam width for the SFG beam using the second-moment of width definition:

$$w_{SFG}^2(l) = 2\frac{\int_0^\infty rdr\int_0^{2\pi} r^2|E_{SFG}(r,\theta)|^2 d\theta}{\int_0^\infty rdr\int_0^{2\pi}|E_{SFG}(r,\theta)|^2 d\theta} \tag{20}$$

Note that we utilize the complex field amplitude of the SFG beam at its waist plane, as presented in Eq. (19), into Eq. (20) to compute the beam width. This is fairly simple, yet provides us an analytical expression that directly relates the SFG beam size with the TC. After substituting Eq. (19) into Eq. (20), and evaluating the angular and radial integrals, we obtain:

$$w_{SFG}(l) = w_0\sqrt{\frac{4n+2|l|+2}{2(\delta n+1)}} \tag{21}$$

Therefore, for a fixed value of n, δ, and w_0, $w_{SFG}(l) \propto \sqrt{|l|}$. We also expect this relationship to hold true at any propagation distance past the beam waist plane. Such a beam characteristic in the propagation dynamics of vortices in different media was reported multiple times in the past. Additionally, the secondary off-axis ring becomes more

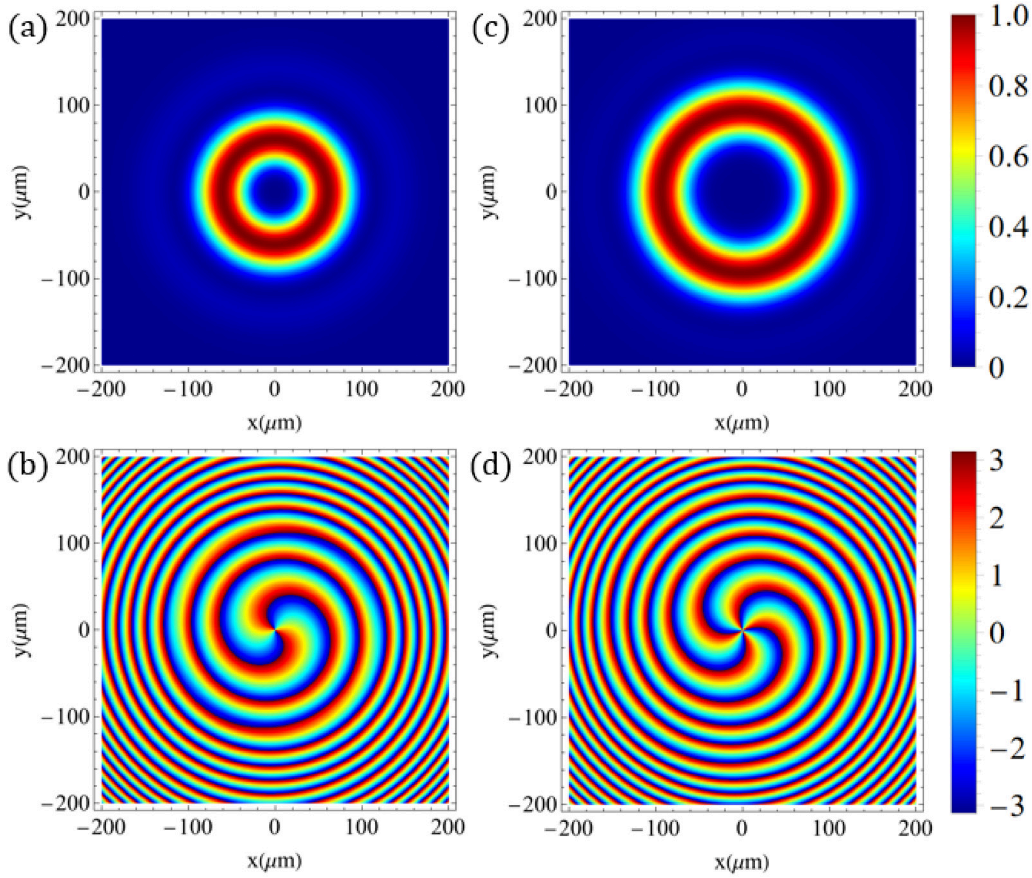

Fig. 4. Transverse intensity and phase distributions of the SFG beam at a propagation distance, $z = 5000$ μm. In (a)–(b) $l_1 = l_2 = 1$, $n_1 = n_2 = 1$, $\delta_1 = \delta_2 = 1$, and in (c)–(d) $l_1 = l_2 = 2$, $n_1 = n_2 = 1$, $\delta_1 = \delta_2 = 1$. As the TC increases, the beam size, dark-core size, and radius of the maximum intensity ring all increase. The intensity colorbar is normalized to the respective maximum value for each panel.

faint upon increasing the TC values (see Fig. 4(c)). Such a feature was demonstrated earlier in the linear propagation of MAV beams in free-space and gradient-index media (Al-Ahsab et al., 2024; Das et al., 2025d). However, in the non-perturbative interaction of ultrashort intense MAV beams with atomic targets, it was demonstrated that higher-order harmonics (17th harmonic to be more specific) display a single-bright intensity ring under these conditions i.e., $l = 1$, $n = 1$, and $\delta = 1$ (Das et al., 2025a). These comparisons between perturbative MAV beams-crystal and non-perturbative MAV beam-atomic gas interactions clearly depict how nonlinear responses of different targets to input MAV beams alter across interaction regimes. From Fig. 4(a) and (c), we also notice that the radius of the maximum intensity ring grows as the TC values of the input MAV beams increase. To understand this behavior, we compute the radius of the maximum intensity ring (r^{SFG}_{max}) for the SFG beam by setting $\frac{\partial |E_{SFG}(r,\theta)|^2}{\partial r} = 0$, and solve it for r^{SFG}_{max}. We find that $r^{SFG}_{max} = w_0\sqrt{\frac{2n_1+2n_2+|l_1|+|l_2|}{2(\delta_1 n_1+\delta_2 n_2+2)}}$. Note that this expression of r^{SFG}_{max} is derived by substituting Eq. (4) into $\frac{\partial |E_{SFG}(r,\theta)|^2}{\partial r} = 0$ for identical values of $w_{0,1}$ and $w_{0,2}$. For identical values of the TC, beam order, and modification parameter of the input MAV beams, $r^{SFG}_{max} = w_0\sqrt{\frac{4n+2|l|}{4(\delta n+1)}}$. Therefore, for a fixed value of n and δ, $r^{SFG}_{max} \propto \sqrt{|l|}$. It is also important to note although the above relation is derived for the SFG beam at the waist plane, it holds true at different propagation distances as well. It is also important to note that, although the SFG beam intensity is shown on a normalized scale in Fig. 4(a) and (c), the actual beam intensity is relatively higher in the earlier case due to its smaller beam size.

From the transverse phase distributions shown in Fig. 4(b) and (d), we extract the TC information of the SFG beam by simply counting the number of 2π phase shifts along the beam's azimuth, which turns out to be 2 and 4, respectively. These values clearly establish the OAM selection rule, $l_{SFG} = l_1 + l_2$, for the SFG process. Additionally, the selection rule for the energy in the SFG process can be expressed as: $\Omega_3 = \Omega_1 + \Omega_2$. Similar selection rules for the OAM, and energy i.e., $l_q = Ml_1 + Nl_2$, and $\Omega_q = M\Omega_1 + N\Omega_2$ have also been established in the non-perturbative process of HHG driven by two vortex beams, where l_q, and Ω_q are the OAM, and energy of the harmonic order q, l_1, and l_2 are OAMs of the driving vortex beams, and M, and N are the number of photons absorbed from different channels i.e., vortex modes with OAMs l_1, and l_2, respectively. Interestingly, in the HHG process under the dipole limit, different combination of photon absorption pathways give rise to more involved OAM distributions for a given harmonic order, while making sure that the total number of photons absorbed via the interaction is an odd number. Therefore, the HHG process can be thought of as a higher-order frequency mixing process. Additionally, we observe spiraling in the phase structure as the SFG beam propagates beyond its waist plane (see Fig. 4(b), and (d)). The z-dependent phase terms present in Eq. (12) along with the helical phase induce such spiraling.

In Fig. 4(a) and (c), we show the transverse intensity distributions of the SFG beam only at a specific propagation distance i.e., $z = 5000$ μm. However, from an application perspective, it is important to thoroughly understand how the short-wavelength SFG beam evolves in free-space. Does it follow similar propagation trajectories as the fundamental MAV beam? Therefore, we analyze the propagation dynamics of the SFG

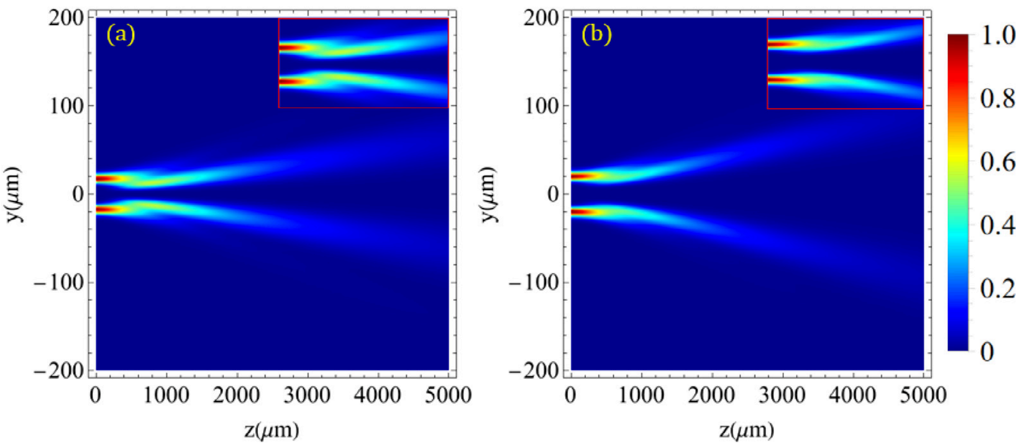

Fig. 5. Longitudinal intensity distributions of the SFG beam. In (a) $l_1 = l_2 = 1$, $n_1 = n_2 = 1$, $\delta_1 = \delta_2 = 1$, and in (b) $l_1 = l_2 = 2$, $n_1 = n_2 = 1$, $\delta_1 = \delta_2 = 1$. At short propagation distances, non-diffracting behavior is evident in both beams, while self-focusing becomes prominent at intermediate distances and diffraction dominates at long distances. Additionally, the SFG beam with a higher TC exhibits greater divergence than the SFG beam with a relatively lower TC. The intensity colorbar is normalized to the respective maximum value for each panel.

beam carrying different TCs in free-space and the results are shown in Fig. 5. Owing to the circular symmetry of the SFG beam, we set one transverse dimension to zero (i.e., $x = 0$ in our simulation) and illustrate the beam evolution along the other transverse dimension (i.e., y) as a function of the propagation distance. An equivalent result would be obtained if the analysis were performed with $y = 0$. For $l_1 = l_2 = 1$, as displayed in Fig. 5(a), it can be seen that the SFG beam maintains its beam size and intensity until a short propagation distance beyond the waist plane. Later, the beam undergoes self-focusing phenomena, where the beam profile size significantly decreases along with a sharp enhancement in the beam intensity. Additionally, a secondary off-axis ring appears in the self-focusing stage. When the beam propagates further to larger distances, it diffracts, where the beam size spreads and the beam intensity decreases monotonically with increasing propagation distances. When the TC values are increased to $l_1 = l_2 = 2$, one can clearly observe the extension in the dark-core and beam sizes of the SFG beam, both at the waist plane as well as at different propagation distances (see Fig. 5(b)). Propagation features, such as maintenance of the beam size and intensity for short propagation distances, appearance of self-focusing and diffraction effects at distinct propagation distances are also observed in this scenario. Additionally, it can also be observed that the secondary off-axis ring eventually faints and disappear upon the propagation of the beam to larger distances, consistent with what we see in Fig. 4(c). Moreover, the self-focusing point moves away from the waist plane for increasing TC values (see Fig. 5(a)–(b)). The divergence is greater for the SFG beam with a higher TC than for the SFG beam with a relatively lower TC. It is important to highlight that fundamental MAV beams exhibit similar propagation properties.

In Fig. 6, we present the longitudinal intensity distributions of the SFG beam generated via sum-frequency mixing of two conventional LG beams. This analysis is crucial for understanding how different input beam configurations affect the SFG process and the subsequent free-space propagation dynamics of the SFG beam. For this purpose, we set $n_1 = n_2 = 0$ and $\delta_1 = \delta_2 = 0$ in Eqs. (4)–(5) and propagate the resulting SFG beam in free-space. The wavelengths used are $\lambda_1 =$ 775 nm, and $\lambda_2 = 1550$ nm. Fig. 6(a) shows the longitudinal intensity distribution when both input LG beams carry TCs $l_1 = l_2 = 1$. The SFG beam exhibits non-diffracting propagation only up to its Rayleigh range, beyond which diffraction becomes evident. In the far-field, the beam size broadens, the dark core expands, and the beam intensity progressively decreases. When the TCs of the input beams are increased to $l_1 = l_2 = 2$, as depicted in Fig. 6(b), the beam intensity at the generation plane is reduced, and both the beam size and the dark-core size become larger compared to Fig. 6(a). Nevertheless, the SFG beam retains similar propagation characteristics to those described in Fig. 6(a). Additionally, in the far-field, the SFG beam with a higher TC exhibits greater divergence — a trend also observed in Fig. 5 for SFG beams produced through frequency mixing of MAV beams. A comparison between Figs. 5 and 6 shows that, in both beam configurations, non-diffracting propagation over short distances and the predominant effect of diffraction at larger distances are present. However, the self-focusing of the SFG beam observed at intermediate distances in Fig. 5 is completely absent in Fig. 6. This behavior is expected, as input LG beams do not exhibit self-focusing in free-space, whereas input MAV beams do. Consequently, we conclude that the propagation dynamics of the SFG beam are shaped by the choice of the input beam configuration.

In Fig. 7(a), we study how the TC of the input MAV beams affects the power of the SFG beam at the waist plane. Note that we use Eq. (17) to plot the SFG beam power as a function of the input MAV beam power. For this analysis, we use: $P_{0,1} = P_{0,2} = P_0 = 15$ W, $w_{0,1} = w_{0,2} = w_0 = 20$ μm, $n_1 = n_2 = n = 1$, $\delta_1 = \delta_2 = \delta = 1$, and three different values of the TC i.e., $l = 1, 2$, and 3. From the figure, a clear quadratic scaling between the SFG beam power and input MAV beam power can be observed. Additionally, it can be clearly seen that the SFG beam power decreases monotonically with increasing TCs of the MAV beam. This behavior is easily understandable since an increase in the TC leads to an enhancement in the beam size, which in turn, reduces the power (or, intensity) of the SFG beam. Such a trend was reported earlier in the SHG process driven by LG vortex beams in a KTP crystal (Das et al., 2025e). In Ref. Das et al. (2025e), it was further discussed how such a novel property could be exploited to improve lateral resolution in stimulated-emission depletion microscopy — a super resolution microscopy technique. Additionally, in Fig. 7(b) and (c), we present the power of the SFG beam generated through frequency mixing of traditional AV beams ($n_1 = n_2 = n = 1$, $\delta_1 = \delta_2 = \delta = 0$) and LG beams ($n_1 = n_2 = n = 0$, $\delta_1 = \delta_2 = \delta = 0$). To enable a direct one-to-one comparison, we employ the same waist sizes, crystal length as those used for the MAV beams. This comparison is crucial for demonstrating the potential advantages of using MAV beams over other vortex beam types in the SFG process. As can be seen from Fig. 7(b) and (c), for a given TC, the SFG beam power increases with increasing input beam power. Conversely, for a fixed input beam power, the SFG beam power decreases as the TC increases. These trends are fully consistent with those observed for MAV beams in Fig. 7(a). However, a comparison across Fig. 7(a)–(c) reveals that, for a fixed TC and increasing input beam power, the SFG beam power is consistently higher for MAV beams than for traditional AV and LG beams. This leads us to conclude that the conversion efficiency of the SFG process can indeed be enhanced

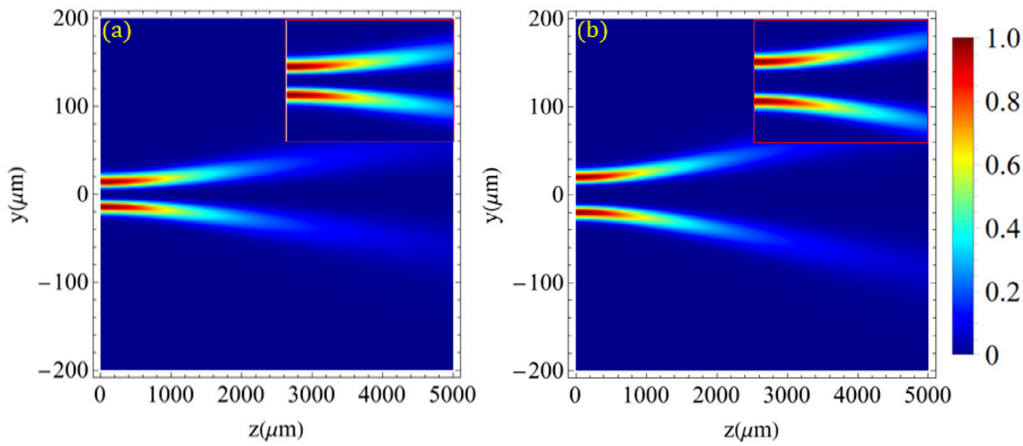

Fig. 6. Longitudinal intensity distributions of the SFG beam generated from the frequency-mixing of two LG beams. In (a) $l_1 = l_2 = 1$, $n_1 = n_2 = 0$, $\delta_1 = \delta_2 = 0$, and in (b) $l_1 = l_2 = 2$, $n_1 = n_2 = 0$, $\delta_1 = \delta_2 = 0$. As the TC increases, the intensity of the SFG beam decreases, its beam size broadens, and the dark-core expands. In contrast to the SFG beam generated through sum-frequency mixing of MAV beams, this SFG beam does not exhibit self-focusing behavior. Moreover, the divergence of the SFG beam is greater for higher TCs than for lower ones. The intensity colorbar is normalized to the respective maximum value for each panel.

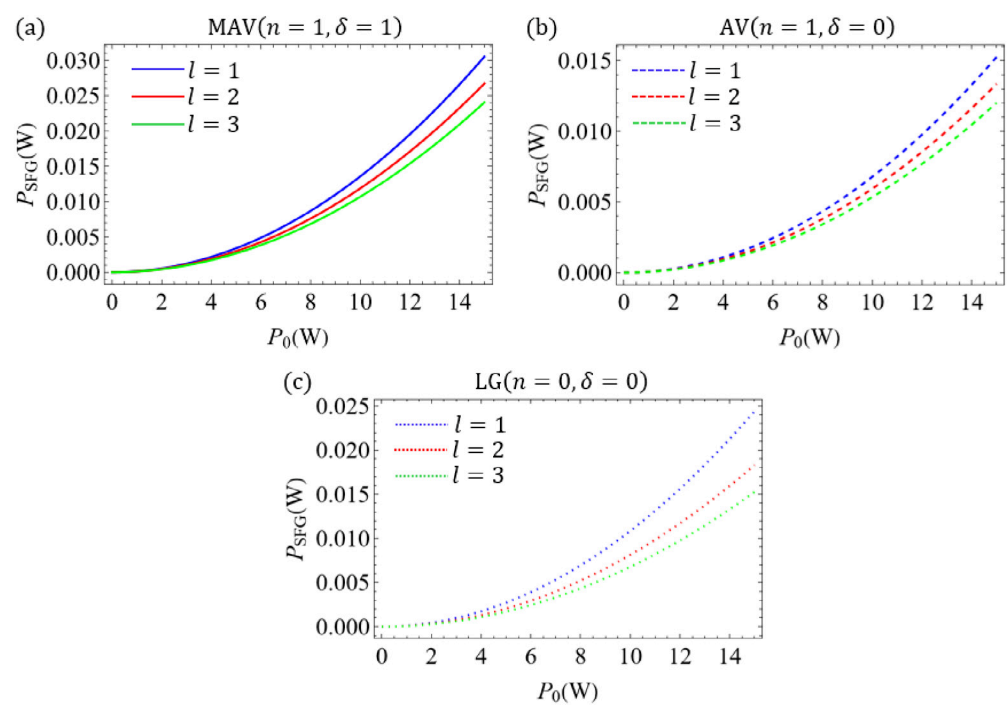

Fig. 7. Comparison of the SFG beam power as a function of the fundamental beam's power for TCs $l = 1, 2$, and 3. The results are presented in (a) for an MAV beam with parameters $n = 1$, $\delta = 1$; in (b) for a traditional AV beam with parameters $n = 1$, $\delta = 0$; and in (c) for an LG beam with parameters $n = 0$, $\delta = 0$. A similar trend in the SFG beam power is observed across all three beam types.

by utilizing MAV beams. It is also worth noting that the SFG beam power is relatively higher for LG beams than for their traditional AV counterparts (where $\delta = 0$). This observation clearly highlights the crucial role of the modification parameter in governing the SFG beam power and, consequently, the conversion efficiency of the SFG process.

In Fig. 8, we present the conversion efficiency of the SFG process as a function of the nonlinear crystal length for different TCs and beam types: (a) MAV beam ($n_1 = n_2 = n = 1$, $\delta_1 = \delta_2 = \delta = 1$), (b) traditional AV beam ($n_1 = n_2 = n = 1$, $\delta_1 = \delta_2 = \delta = 0$), and (c) LG beam ($n_1 = n_2 = n = 0$, $\delta_1 = \delta_2 = \delta = 0$). This analysis is primarily based on Eq. (18). As expected, Fig. 8 exhibits quadratic curves, which arise from the quadratic dependence of the conversion efficiency on the crystal length ($\eta \propto L^2$ in Eq. (18)). Interestingly, this quadratic behavior is not exclusive to vortex beams. It has also been observed in perturbative nonlinear optical processes driven by Gaussian beams, such as SHG and SFG. Furthermore, this trend is anticipated to change when a nonzero phase-mismatch factor is included in the calculations. In such cases, instead of a simple quadratic increase, the SFG beam power and conversion efficiency may exhibit oscillatory behavior with a period proportional to the coherence length. As can be seen from Fig. 8(a), for a fixed TC, the efficiency increases with crystal length. However, at a given crystal length, the efficiency is higher for MAV beams with lower TCs. This behavior becomes even more apparent as we increase the crystal length. A similar trend is observed in Fig. 8(b) and (c) for traditional AV and LG beams. Importantly, comparing Fig. 8(a)–(c) reveals that under identical conditions, the conversion efficiency is always higher when MAV beams drive the SFG process

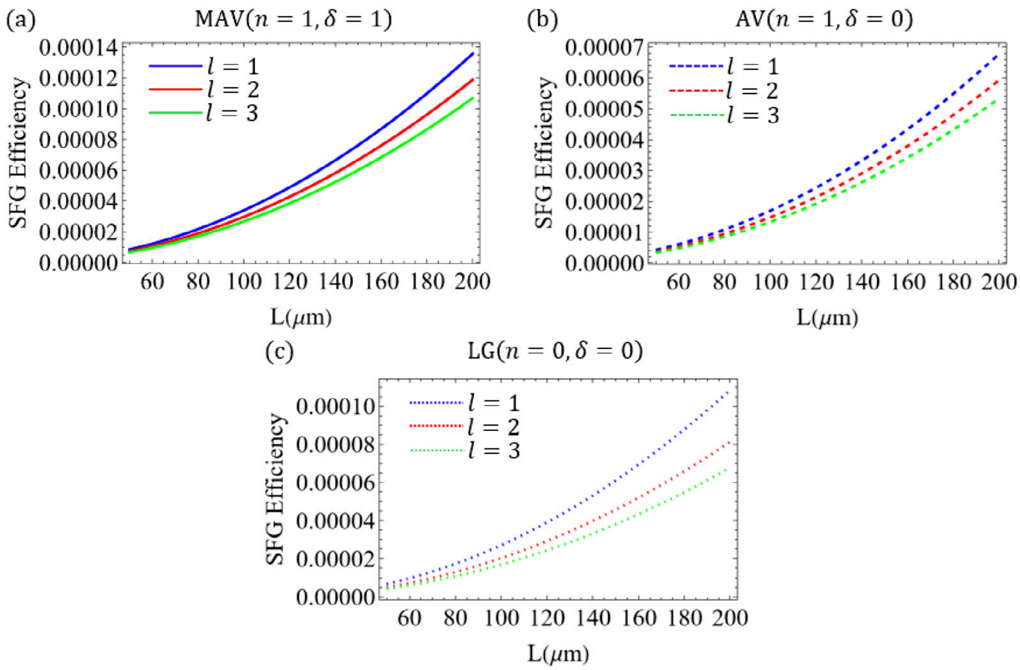

Fig. 8. Comparison of the conversion efficiency as a function of the nonlinear crystal length for TCs $l = 1, 2$, and 3. The results are presented in (a) for an MAV beam with parameters $n = 1$, $\delta = 1$; in (b) for a traditional AV beam with parameters $n = 1$, $\delta = 0$; and in (c) for an LG beam with parameters $n = 0$, $\delta = 0$. A similar trend in the conversion efficiency is observed across all three beam types.

compared to traditional AV and LG beams. Moreover, the efficiency of the SFG process driven by LG beams is higher than that driven by AV beams. Collectively, these results highlight the critical role of the modification parameter in controlling the conversion efficiency of the SFG process and underscore the advantage of using MAV beams to drive the process.

3.2. Case 2: $l_1 \neq l_2$, $n_1 = n_2$ (small), $\delta_1 = \delta_2$

In this case, we choose distinct TC values ($l_1 \neq l_2$) for the input MAV beams, while keeping their beam order and modification parameter values fixed i.e., $n_1 = n_2 = 1$ and $\delta_1 = \delta_2 = 1$, as considered in the previous case. In Fig. 9(a) and (b), we present the transverse intensity and phase distributions of the SFG beam for TCs $l_1 = 1, l_2 = 2$ at a distance $z = 5000$ μm. The intensity profile shown in Fig. 9(a) consists of a bright ring surrounded by a less-intense ring. However, a comparison between Fig. 4(a) ($l_1 = 1, l_2 = 1$) and Fig. 9(a)($l_1 = 1, l_2 = 2$) reveals that the overall beam size is bigger in the latter case. This can be easily understood if we calculate the TC-dependent beam width of the SFG beam for the scenario, when TCs of the input MAV beams are distinct, although their beam order and modification parameter values are identical. After substituting Eq. (4) into Eq. (20), and solving it for identical values of n and δ, we obtain:

$$w_{SFG}(l) = w_0 \sqrt{\frac{4n + |l_1| + |l_2| + 1}{2(\delta n + 1)}} \tag{22}$$

Eq. (22) clearly reveals that the beam size is usually bigger for larger values of $|l_1| + |l_2|$. Although Eq. (22) is derived by considering the SFG beam at its waist plane, this relationship also holds true at different propagation distances beyond the waist plane. The value of $|l_1| + |l_2|$ is equal to 2 in Fig. 4(a), whereas it is equal to 3 in Fig. 9(a). Similarly, when we set the TC values to $l_1 = 1, l_2 = 4$ as shown in Fig. 9(c), we notice a further enhancement in the SFG beam size as compared to that reported in Fig. 9(a), following the relationship in Eq. (22). Additionally, with increasing TC values, the secondary off-axis ring becomes so weak that it is hardly visible in the intensity distribution, as displayed in Fig. 9(c). We also observe an enhancement in the radius of the maximum intensity ring with increasing TC values of the input MAV beams following the relation, $r_{max}^{SFG} \propto \sqrt{|l_1| + |l_2|}$, derived earlier in Case 1. A comparison of the SFG beam intensity in Fig. 9(a) and (c) shows that the intensity is higher in the former, owing to its smaller beam size. The generation of short-wavelength MAV beam – via the SFG process – exhibiting high TC, controllable dark-core size and intensity rings could be extremely useful in the efficient trapping of microscopic particles.

From the phase distributions, we find that there are $3 \times 2\pi$ and $5 \times 2\pi$ phase shifts along the beam's azimuth, as shown in Fig. 9(b) and (d), respectively. This is clearly in accordance with the OAM selection rule, $l_{SFG} = l_1 + l_2$ for the SFG process. To experimentally measure the TC of the SFG beam, one can simply adopt a self-referenced interferometric technique. In this technique, the SFG beam, whose TC is to be measured, is interfered with its own mirror image. A dove prism can be used to create the mirror image of the SFG beam, provided the beam is not tightly focused i.e., the beam description should follow the paraxial limit and the wavelength of the beam must lie beyond the extreme-ultraviolet range (since extreme-ultraviolet light will be completely absorbed by the prism material). The mirror image of the SFG beam shows the opposite sense of rotation, so $\exp(-il_{SFG}\theta')$ in Eq. (12) transforms to $\exp(il_{SFG}\theta')$. Consequently, the phase difference becomes $\exp(i2l_{SFG}\theta')$. As a result, one would observe $2l_{SFG}$ number of petals in the interference pattern. By counting the number of petals and dividing the outcome by a factor of two provides the information about the TC of the SFG beam. An alternative approach to measure the TC of the SFG beam would be to illuminate a cylindrical lens with the SFG beam, and counting the number of minima between the maximum intensity lobes in the transformed Hermite-Gaussian intensity pattern. The number of minima is exactly related to the TC of the illuminating beam.

In Fig. 10, we show the longitudinal intensity distributions of the SFG beam, when the TCs of the input MAV beams are different. Fig. 10(a) displays the intensity distribution, when $l_1 = 1, l_2 = 2$. For a short propagation distance, the beam exhibits non-diffracting characteristic

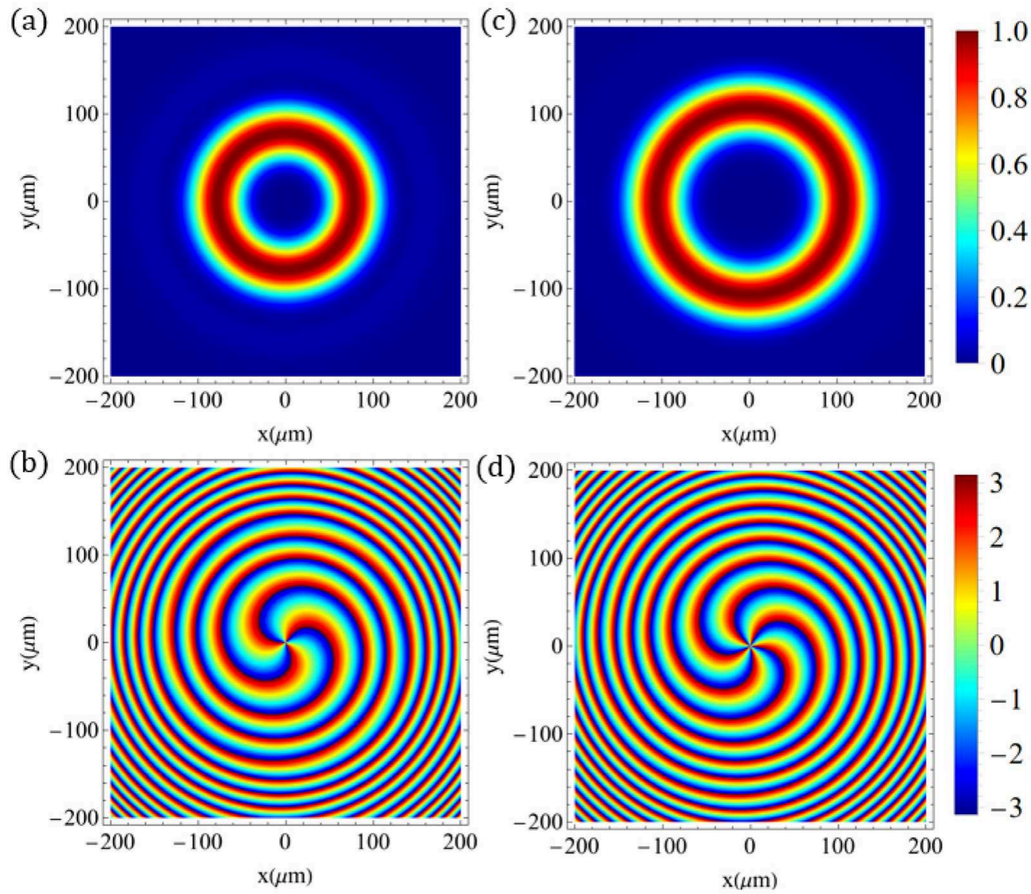

Fig. 9. Transverse intensity and phase distributions of the SFG wave at a propagation distance, $z = 5000$ μm. In (a)–(b) $l_1 = 1, l_2 = 2$, $n_1 = n_2 = 1$, $\delta_1 = \delta_2 = 1$, and in (c)–(d) $l_1 = 1, l_2 = 4$, $n_1 = n_2 = 1$, $\delta_1 = \delta_2 = 1$. Similar to Fig. 4, increasing the TC results in a larger beam size and a broader dark-core, accompanied by a decrease in beam intensity. Moreover, for higher TCs of the input MAV beams, the less intense ring becomes almost invisible. The intensity colorbar is normalized to the respective maximum value for each panel.

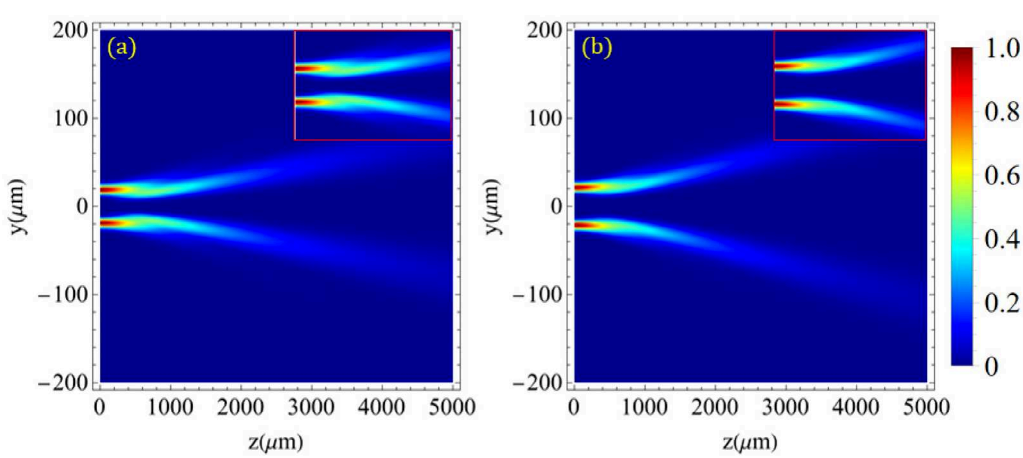

Fig. 10. Longitudinal intensity distributions of the SFG beam. In (a) $l_1 = 1, l_2 = 2$, $n_1 = n_2 = 1$, $\delta_1 = \delta_2 = 1$, and in (b) $l_1 = 1, l_2 = 4$, $n_1 = n_2 = 1$, $\delta_1 = \delta_2 = 1$. Similar behavior to that reported in Fig. 5 is also observed here, including non-diffracting propagation at short distances, self-focusing at intermediate distances, and diffraction effects in the far-field. The intensity colorbar is normalized to the respective maximum value for each panel.

following which it undergoes self-focusing. However, the secondary off-axis ring surrounding the bright intensity ring is very weak and hardly visible in the self-focusing stage. When the beam propagates to larger distances, the beam size spreads due to diffraction and the dark-core size expands along with a reduction in the beam intensity. In Fig. 10(b), we show the intensity distribution for $l_1 = 1, l_2 = 4$. As expected from Eq. (22), the beam size expands with increasing TC values, when compared to Fig. 10(a). The beam maintains its profile size and intensity for a short propagation distance. However, the self-focusing effect becomes less prominent in this scenario. Additionally, the intensity of the secondary off-axis ring reduces so much that it is no longer visible in the intensity distribution. An enhancement in the TC value is solely responsible for such a behavior of the SFG beam. Similar to Case 1, we also note that the SFG beam with a relatively

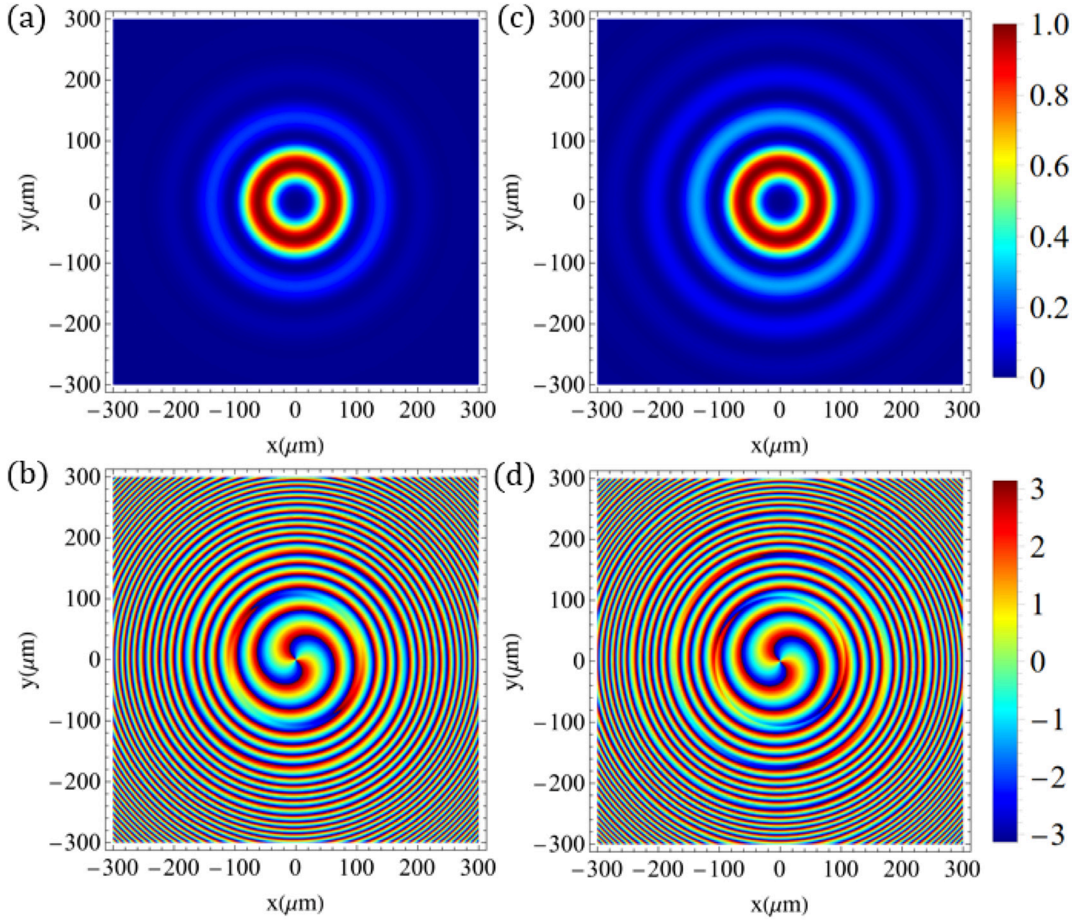

Fig. 11. Transverse intensity and phase distributions of the SFG wave at a propagation distance, $z = 5000$ μm. In (a)–(b) $l_1 = l_2 = 1$, $n_1 = n_2 = 4$, $\delta_1 = \delta_2 = 1$, and in (c)–(d) $l_1 = l_2 = 1$, $n_1 = n_2 = 10$, $\delta_1 = \delta_2 = 1$. Increasing the beam order of the input MAV beams leads to a greater number of secondary off-axis rings in the intensity distribution of the SFG beam. The intensity colorbar is normalized to the respective maximum value for each panel.

higher TC exhibits greater divergence in the far-field. We can conclude that for smaller beam order values of the input MAV beams, their TCs play a pivotal role in shaping the spatial structure of the SFG beam both at its waist plane and beyond.

3.3. Case 3: $l_1 = l_2$, $n_1 = n_2$ (large), $\delta_1 = \delta_2$

In this case, we investigate the impact of using higher beam order values for the input MAV beams on the intensity and phase distributions of the SFG beam. To this end, we fix the values of the TC and modification parameter to $l_1 = l_2 = 1$ and $\delta_1 = \delta_2 = 1$, while the beam order values are set to $n_1 = n_2 = 4$ in Fig. 11(a)–(b), and $n_1 = n_2 = 10$ in Fig. 11(c)–(d). Furthermore, the transverse intensity and phase distributions are shown at a distance of $z = 5000$ μm. From Fig. 11(a), we observe that there exists at least two secondary off-axis rings in the intensity distribution, apart from the maximum intensity ring. A comparison between Fig. 4(a) ($n_1 = n_2 = 1$) and Fig. 11(a) ($n_1 = n_2 = 4$) reveals that: (1) an increase in the beam order values lead to more intensity rings for the SFG beam, (2) for identical values of the TC and modification parameter of the input MAV beams, the SFG beam size expands with increasing beam order values. To understand the latter result better, we compute the size of the SFG beam by plugging Eq. (4) into Eq. (20) for distinct beam order values, and we obtain:

$$w_{SFG}(l) = w_0 \sqrt{\frac{2n_1 + 2n_2 + 2|l| + 1}{\delta(n_1 + n_2) + 2}} \tag{23}$$

If we substitute $n_1 = n_2 = 1$ (as considered in Fig. 4(a)), and $n_1 = n_2 = 4$ (as considered in Fig. 11(a)), $w_{SFG}(l)$ is greater for the latter case. This conclusion holds true at any propagation distance past the beam waist plane. In Fig. 11(c), we change the values of n_1 and n_2 to 10, while maintaining the same values of the TC and modification parameter as used in Fig. 11(a). It can be noticed that as the beam order values further increase, we see more off-axis rings in the intensity distribution, when compared to Fig. 11(a). Additionally, the beam size of the SFG beam increases with beam order following Eq. (23). The radius of the maximum intensity ring is slightly higher in Fig. 11(c), when compared with Fig. 11(a), following the expression of r_{max} derived in Case 1 for identical values of the TC, beam order, and modification parameter of input MAV beams. A comparison between the fundamental MAV beam and the SFG beam reveals an interesting conclusion: for fixed values of the TC and modification parameter, the beam size is larger for lower values of the beam order (see Figs. 1, 2, and 3). However, for the SFG beam, the beam size grows monotonically with increasing beam order values of input MAV beams (see Figs. 11, and 12). Therefore, we can conclude that the nonlinearity of the SFG process alters the fundamental characteristics of the beam. It is important to highlight that the appearance of multiple off-axis rings in the frequency up-converted extreme ultraviolet radiation was reported earlier, when the MAV beam engineered with higher beam order drove the HHG process in atomic targets (Das et al., 2025a). For example, in Ref. Das et al. (2025a), it was demonstrated that the 17th harmonic order contains a single secondary off-axis ring for $n = 10$, and $l = 1$ of the fundamental MAV beam. However, as the TC increases from $l = 1$ to

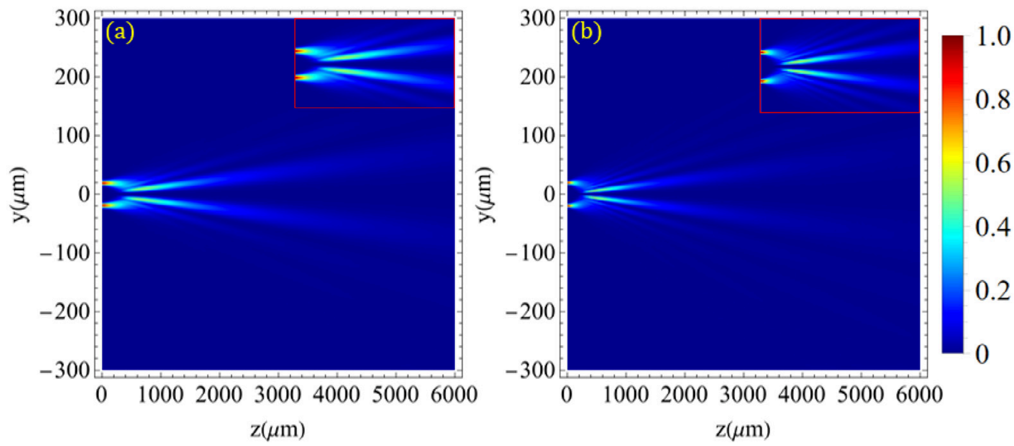

Fig. 12. Longitudinal intensity distributions of the SFG wave. In (a) $l_1 = l_2 = 1$, $n_1 = n_2 = 4$, $\delta_1 = \delta_2 = 1$, and in (b) $l_1 = l_2 = 1$, $n_1 = n_2 = 10$, $\delta_1 = \delta_2 = 1$. For higher beam order values, the self-focusing region shifts closer to the beam waist plane. The intensity colorbar is normalized to the respective maximum value for each panel.

$l = 5$, the secondary off-axis ring disappears from the far-field intensity distribution. In the present case, we observe more than one secondary off-axis ring for the SFG beam, when $l_1 = l_2 = 1$ and $n_1 = n_2 = 10$. These distinctions clearly depict the pivotal role of the nature (perturbative or non-perturbative) of the nonlinear optical process. Additionally, such features were also reported in the linear propagation of the MAV beam in gradient-index media. The phase distributions in Fig. 11(b) and (d) supports the OAM conservation rule in the SFG process i.e., $l_{SFG} = l_1 + l_2$, although the phase structures are more intricate in this case, when compared with Case 1 and Case 2. The phase structures also provide information about the presence of secondary off-axis rings in their corresponding intensity distributions.

In Fig. 12(a) and (b), we show the longitudinal intensity distributions of the SFG beam, for $n_1 = n_2 = 4$ and $n_1 = n_2 = 10$, respectively. Both non-diffracting and self-focusing effects are observed in all the scenarios. Additionally, in both scenarios, we notice the influence of diffraction on the SFG beam propagation at larger distances. However, we see more off-axis rings in the latter case due to higher beam order values. An interesting conclusion can be made in the context of how TC and beam order values control the number of off-axis rings in the SFG beam: for identical beam order values of the input MAV beams, the effect of increasing TC values is to faint the secondary off-axis ring of the SFG beam, which eventually disappears. However, for identical TC values of the input MAV beams, the number of secondary off-axis rings in the SFG beam grows as the beam order values of input MAV beams increase. Furthermore, the self-focusing region shifts towards the beam waist plane i.e., $z = 0$ for increasing beam order values (see Fig. 12(a) and (b)). Such a propagation property was also reported in the propagation of the MAV beam in gradient-index media (Das et al., 2025d). Here, we would like to make an interesting comparison between POV beams and the SFG beam generated by MAV beams: (1) For POV beams, increasing the ratio of their ring radius (R) to half-ring width (w_p) increases the number of secondary off-axis rings in the self-focusing region (Wang et al., 2023; Kumar Das et al., 2025d; Das et al., 2025c), whereas, increasing the beam order values of input MAV beams gives rise to more off-axis rings in the SFG beam's case. (2) For POV beams, reduction in the ratio of R/w_p shrinks the self-focusing region and the self-focusing region shifts towards the beam waist plane. However, in the SFG beam's case, reduction in the beam order values of MAV beams shifts the self-focusing region farther away from the beam waist plane.

3.4. Case 4: $l_1 = l_2$, $n_1 \neq n_2$ (large), $\delta_1 = \delta_2$

In this case, we choose distinct beam order values for the input MAV beams i.e., $n_1 = 4, n_2 = 10$, and use identical values of the modification parameter i.e., $\delta_1 = 1 = \delta_2$. In Fig. 13(a) and (c), we show the intensity distributions of the SFG beam for $l_1 = l_2 = 1$ and $l_1 = l_2 = 3$, respectively at a distance of $z = 5000$ μm. We observe multiple secondary off-axis rings in both the scenarios, which is obviously due to high beam order values. Moreover, the radius of the maximum intensity ring, the size of the dark-core, and the beam size are larger for the latter case due to its increased TC values. For example, the radius of the maximum intensity ring in this case can be expressed as: $r^{SFG}_{max} = w_0\sqrt{\frac{2n_1+2n_2+2|l|}{2\delta(n_1+n_2)+4}}$. Therefore, for fixed values of n_1, n_2, and δ, $r^{SFG}_{max} \propto \sqrt{|l|}$, which is precisely the case for Fig. 13(a) and (c). Additionally, the outermost off-axis ring becomes weaker with increasing TC values, as discussed in earlier cases. A comparison between Figs. 13(a) and 11(a), (c) reveals that for identical TC and modification parameter values of the input MAV beams, the beam size increases with increasing values of $n_1 + n_2$. From the phase distributions shown in Fig. 13(b) and (d), the OAM selection rule, $l_{SFG} = l_1 + l_2$, can easily be verified by counting the number of 2π phase shifts along the SFG beam's azimuth. Additionally, the transverse phases of the SFG beam become more involved as the beam order values are increased.

From the longitudinal intensity distributions of the SFG beam shown in Fig. 14(a) and (b), we observe non-diffracting and self-focusing characteristics for the beam in both the scenarios. Additionally, we see an enhancement in the beam and dark-core sizes with increasing TC values of the input MAV beams. Moreover, the number of off-axis rings in the self-focusing stage reduces as the TC values increase. Although the beam intensity is presented on a normalized scale, it is relatively lower in Fig. 14(b) than in Fig. 14(a) due to the increase in TC.

3.5. Case 5: $l_1 = l_2$, $n_1 = n_2$ (small), $\delta_1 \neq \delta_2$

In this case, we choose identical values for the TC and beam order of the input MAV beams i.e., $l_1 = l_2 = 1$, and $n_1 = n_2 = 1$, however, select distinct values of the modification parameter for them. The transverse intensity and phase distributions of the SFG beam at a distance $z = 5000$ μm are presented in Fig. 15. A comparison between Fig. 15(a) ($\delta_1 = 1, \delta_2 = 0.7$) and Fig. 15(c) ($\delta_1 = 0.8, \delta_2 = 0.3$) reveals that: (1) the radius of the maximum intensity and the beam size of the SFG beam is slightly higher in the latter case due to its lower modification parameter value, (2) there occurs a single secondary off-axis ring in both the scenarios as the beam order values of input MAV beams are set to

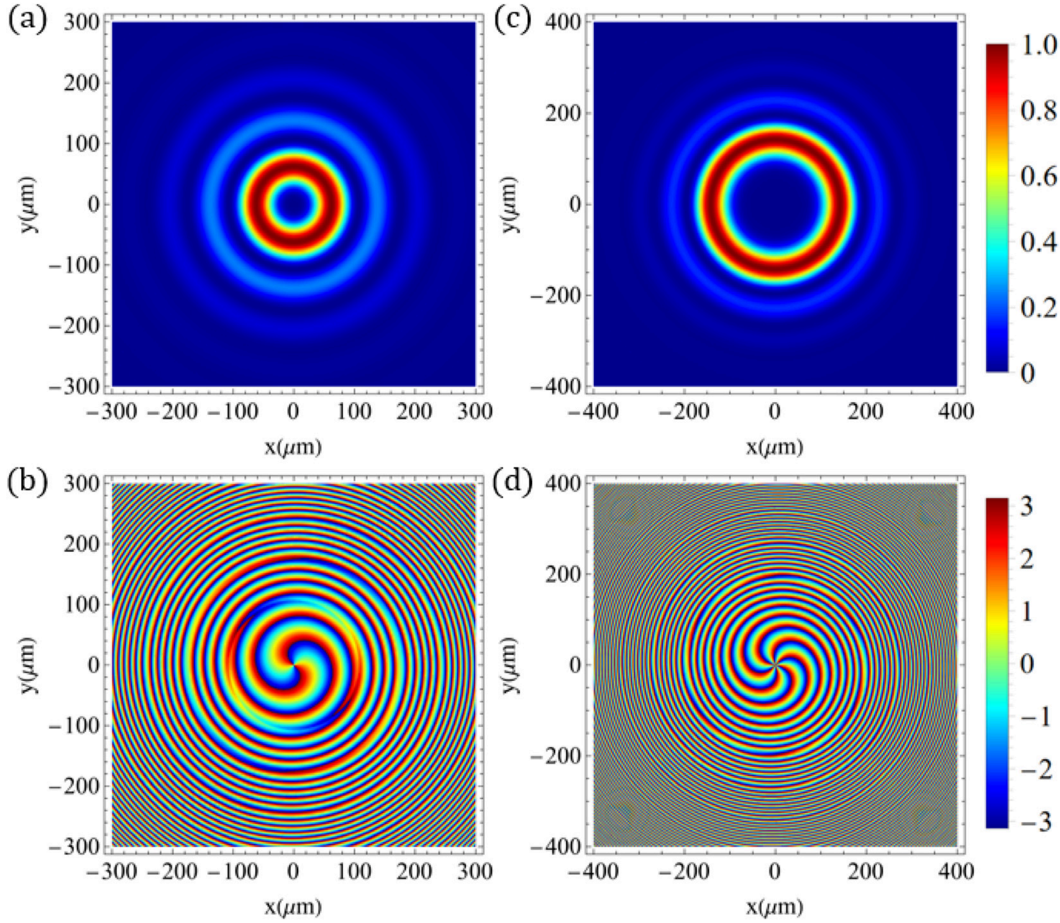

Fig. 13. Transverse intensity and phase distributions of the SFG wave at a propagation distance, $z = 5000$ μm. In (a)–(b) $l_1 = l_2 = 1$, $n_1 = 4, n_2 = 10$, $\delta_1 = \delta_2 = 1$, and in (c)–(d) $l_1 = l_2 = 3$, $n_1 = 4, n_2 = 10$, $\delta_1 = \delta_2 = 1$. For higher-order distinct input MAV beams, secondary off-axis rings emerge in the intensity distribution. As the TC of the input MAV beams increases, both the beam size and the dark-core expand. The intensity colorbar is normalized to the respective maximum value for each panel.

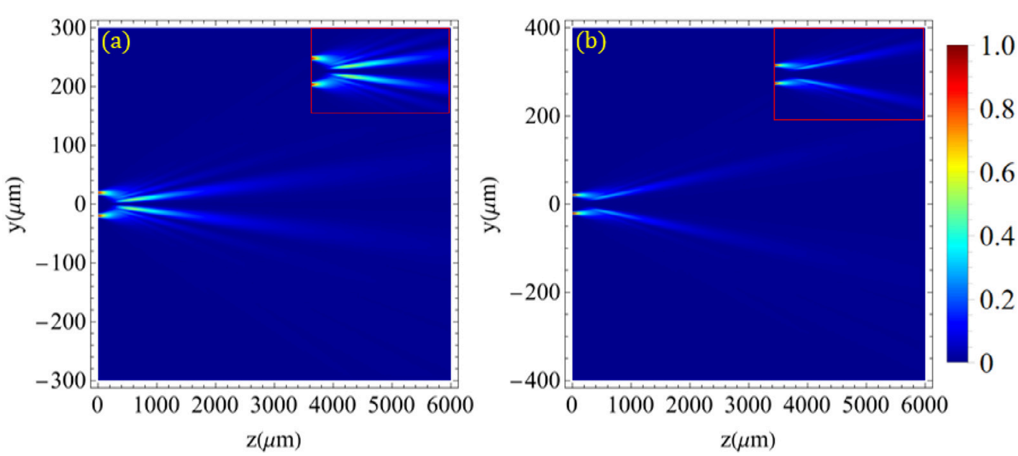

Fig. 14. Longitudinal intensity distributions of the SFG wave. In (a) $l_1 = l_2 = 1$, $n_1 = 4, n_2 = 10$, $\delta_1 = \delta_2 = 1$, and in (b) $l_1 = l_2 = 3$, $n_1 = 4, n_2 = 10$, $\delta_1 = \delta_2 = 1$. The intensity colorbar is normalized to the respective maximum value for each panel.

unity, and (3) the beam intensity is relatively higher in the earlier case. The expansion of the beam size with decreasing modification parameter values follows from the relation:

$$w_{SFG}(l) = w_0 \sqrt{\frac{4n + 2|l| + 1}{n(\delta_1 + \delta_2) + 2}} \tag{24}$$

Therefore, a lower value of $\delta_1 + \delta_2$ gives rise to a higher SFG beam size. From the phase plots displayed in Fig. 15(b) and (d), the number of 2π phase shift is two each, which validates the OAM selection rule, $l_{SFG} = l_1 + l_2$ in the SFG process.

From the longitudinal intensity distributions shown in Fig. 16(a)–(b), we observe both non-diffracting and self-focusing effects in all the scenarios along with the presence of a single secondary off-axis ring.

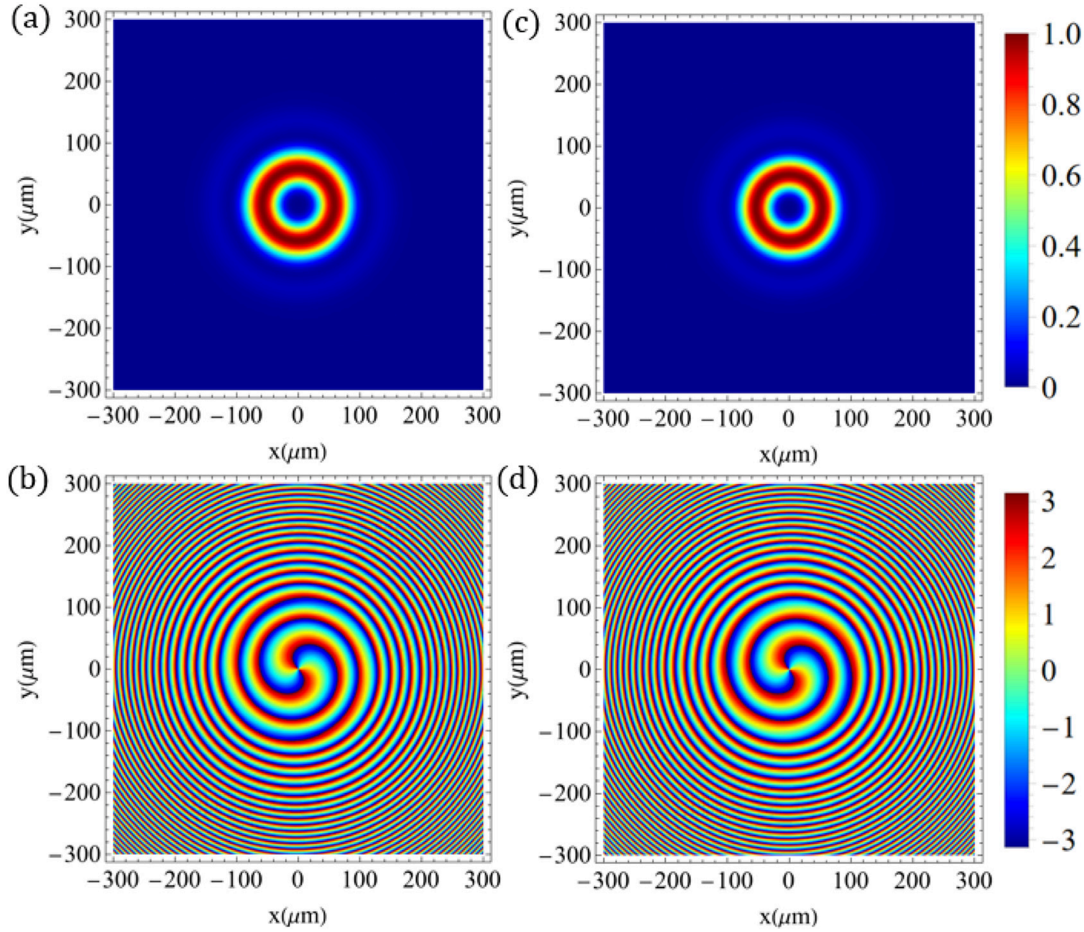

Fig. 15. Transverse intensity and phase distributions of the SFG wave at a propagation distance, $z = 5000$ μm. In (a)–(b) $l_1 = l_2 = 1$, $n_1 = n_2 = 1$, $\delta_1 = 1, \delta_2 = 0.7$, and in (c)–(d) $l_1 = l_2 = 1$, $n_1 = n_2 = 1$, $\delta_1 = 0.8, \delta_2 = 0.3$. Increasing the modification parameter of the input MAV beams reduces the size of the SFG beam. The intensity colorbar is normalized to the respective maximum value for each panel.

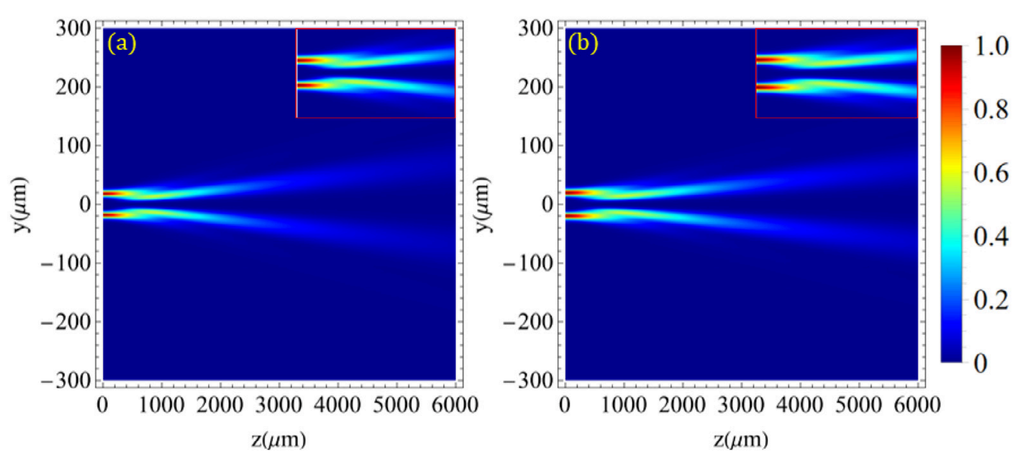

Fig. 16. Longitudinal intensity distributions of the SFG wave. In (a) $l_1 = l_2 = 1$, $n_1 = n_2 = 1$, $\delta_1 = 1, \delta_2 = 0.7$, and in (b) $l_1 = l_2 = 1$, $n_1 = n_2 = 1$, $\delta_1 = 0.8, \delta_2 = 0.3$. The intensity colorbar is normalized to the respective maximum value for each panel.

However, the self-focusing region shifts away from the beam waist plane for decreasing values of the sum of the modification parameters, $\delta_1+\delta_2$. Such a propagation feature was demonstrated in the propagation of the MAV beam in free-space and gradient-index media (Al-Ahsab et al., 2024; Das et al., 2025d).

In our theoretical investigation, the input MAV beams were assigned identical waist sizes – specifically, $w_{0,1} = w_{0,2} = 20$ μm – across all cases considered. It would be worthwhile to examine the effect of varying these waist sizes on the free-space evolution of the SFG beam, particularly in relation to the behavior of its self-focusing point. Previous studies on the free-space propagation of MAV beams have shown that increasing the beam waist size shifts the self-focusing position farther from the waist plane (Al-Ahsab et al., 2024). Likewise, modifying the wavelengths of the input MAV beams could provide further insight into

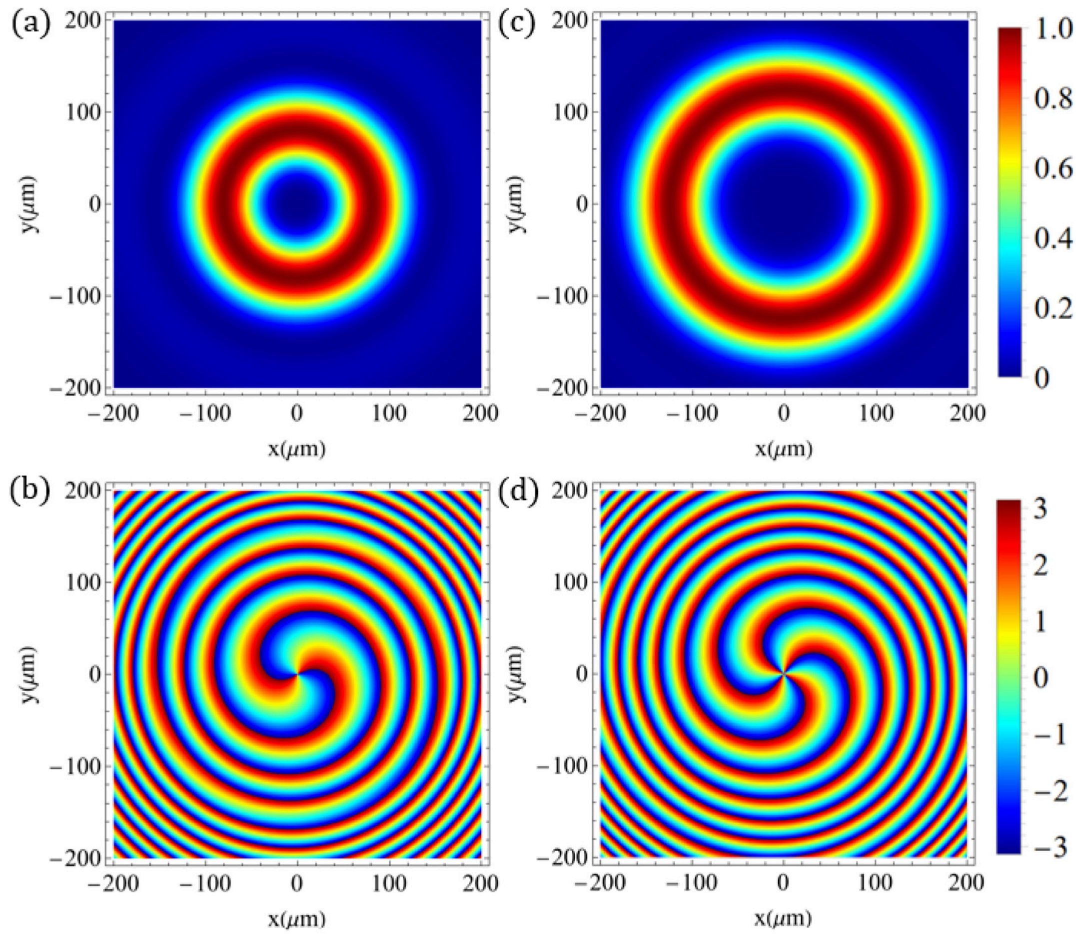

Fig. 17. The same as Fig. 4, except for different wavelengths of the input MAV beams i.e., λ_1 = 1054 nm, and λ_2 = 2000 nm. Increasing the wavelength of the input MAV beams results in greater far-field beam divergence of the SFG beam. The intensity colorbar is normalized to the respective maximum value for each panel.

how the self-focusing point responds, offering additional avenues for optimizing the nonlinear process.

3.6. Case 6: Effect of different wavelengths

From Case 1 to Case 5, we consistently used input MAV beams with wavelengths of λ_1 = 775 nm and λ_2 = 1550 nm to investigate the SFG process in a PPKTP crystal. However, the influence of varying the input MAV beam wavelengths on the propagation dynamics of the SFG beam remains to be explored. From a fundamental perspective, variations in wavelength may affect the far-field beam divergence. To address this, in the present case we increase the input MAV beam wavelengths to λ_1 = 1054 nm and λ_2 = 2000 nm, while keeping all other beam and medium parameters identical to those used in Case 1. The resulting transverse intensity and phase distributions of the SFG beam are shown in Fig. 17 at a propagation distance of z = 5000 μm.

A direct comparison between Figs. 17(a), (c) and 4(a), (c) shows that increasing the input wavelengths of the MAV beams results in a larger beam size (and thus greater beam divergence) in the former case at z = 5000 μm. This outcome is unsurprising and indeed expected, as for identical TC, beam order, waist size, and modification parameter, the far-field beam divergence scales directly with the wavelength of the SFG beam. Note that the SFG beam's wavelength is λ_3 = 690.2 nm in Fig. 17 and 516.6 nm in Fig. 4. Moreover, despite the intensity being normalized in both cases, the SFG beam intensity is relatively lower in Fig. 17(a), (c) than in Fig. 4(a), (c). The phase distributions, presented in Fig. 17(b) and (d), reveal a net TC of 2 and 4, respectively.

In Fig. 18, we present the longitudinal intensity distributions of the SFG beam corresponding to those shown in Fig. 17. As in Case 1, typical free-space propagation features are again observed: the SFG beam exhibits non-diffracting propagation over short distances, followed by self-focusing behavior at intermediate distances, and eventually undergoes diffraction. Furthermore, increasing the TC of the input MAV beams results in an expansion of both the beam and the dark-core sizes, along with a reduction in beam intensity. A comparison between Figs. 18 and 5 shows that self-focusing occurs earlier in Fig. 18 than in Fig. 5. In other words, the self-focusing region shifts toward the beam waist plane as the wavelength of the SFG beam increases. This observation is consistent with the free-space propagation behavior of MAV beams, where a higher wavelength enhances the self-focusing effect, thereby moving the self-focusing region closer to the beam waist plane or the source plane (Al-Ahsab et al., 2024). Additionally, since both the SFG beam power and the conversion efficiency scale inversely with the square of the SFG wavelength, using the longer wavelength in this case (λ_3 = 690.2 nm) results in lower values for both quantities compared to Case 1 (λ_3 = 516.6 nm).

4. Conclusion

In conclusion, we investigated the nonlinear phenomenon of sum-frequency generation (SFG) in a quasi-phase matched PPKTP crystal driven by MAV beams. Under the assumptions of no-pump depletion and ideal phase-matching conditions, we derived an analytical expression for the complex field amplitude of the SFG beam at the waist plane.

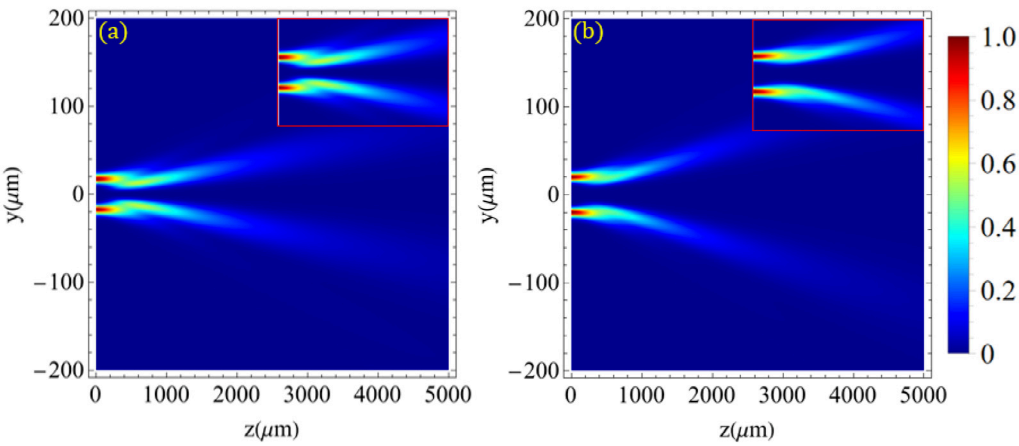

Fig. 18. The same as Fig. 5, except for different wavelengths of the input MAV beams i.e., $\lambda_1 = 1054$ nm, $\lambda_2 = 2000$ nm. A comparison between Figs. 18 and 5 shows that, in the former case, the self-focusing region shifts closer to the beam waist plane. The intensity colorbar is normalized to the respective maximum value for each panel.

Furthermore, employing the Huygens–Fresnel integral in conjunction with the elements of the ABCD matrix enabled us to the derive the free-space complex field amplitude for the SFG beam at a finite propagation distance. We examined the influence of diverse parameters associated with the input MAV beams on both the intensity and phase distributions of the generated SFG beam at a specified propagation distance (transverse profiles), as well as across a range of distances (longitudinal profiles). It was found that: (1) When the modification parameter and beam order values of the input MAV beams are set to unity, both the beam size, the dark-core size, and the radius of the maximum intensity ring of the SFG beam increase with increasing TC values. Additionally, the sole secondary off-axis ring present in the SFG beam's intensity distribution weakens as the TC values increase. (2) With higher beam order values (>1) of the input MAV beams, while keeping identical TC and modification parameter values, the intensity distribution of the SFG beam exhibits an increased number of secondary off-axis rings and its overall size expands. Additionally, the self-focusing region in the SFG beam's propagation moves closer to the beam waist plane. (3) For identical TC and beam order values of the input MAV beams, the beam size and the radius of the maximum intensity ring increase as the sum of the modification parameter values decreases. Furthermore, the self-focusing region moves away from the beam waist plane when the sum of the modification parameter values is reduced. (4) The selection rule governing OAM in SFG, namely, the relation $l_{SFG} = l_1 + l_2$, is consistently supported across all cases examined in our theoretical analysis. (5) The SFG beam power and conversion efficiency decrease as the TC increases — a trend observed for MAV, traditional AV, and LG beams. However, under identical beam and medium parameters, the SFG beam power and conversion efficiency remain consistently higher for MAV-driven SFG compared to that driven by traditional AV or LG beams. (6) An increase in the wavelength of the SFG beam shifts the self-focusing region nearer to the beam waist plane.

In this work, the MAV beams were in the near-infrared spectral range, resulting in an SFG signal within the visible range. However, by selecting MAV beams at visible wavelengths, the SFG output can be extended into the deep-ultraviolet or beyond. Generating short-wavelength MAV beams with high TC and a tunable dark-core size would significantly expand their utility in particle trapping, optical communication, and mode-switching. As a future outlook, it would be interesting to explore SFG driven by POVs and grafted optical vortices (Zhang et al., 2019), as these beams maintain a consistent beam size with changing TC. Such a study would enable a direct comparison of the output power and conversion efficiency with those obtained using MAV beams.

CRediT authorship contribution statement

Bikash K. Das: Writing – review & editing, Writing – original draft, Visualization, Validation, Supervision, Software, Methodology, Investigation, Formal analysis, Data curation, Conceptualization. **Camilo Granados:** Writing – review & editing, Writing – original draft. **Wenlong Gao:** Writing – review & editing, Writing – original draft. **Stephan Fritzsche:** Writing – review & editing, Writing – original draft, Supervision.

Declaration of competing interest

The authors declare that they have no known competing financial interests or personal relationships that could have appeared to influence the work reported in this paper.

Acknowledgments

This research received no external funding.

Data availability

Data will be made available on request.

References

Al-Ahsab, H., Cheng, M., Cao, Y., Zhang, H., Yi, X., Yan, X., Guo, L., 2024. Introduction of a modified anomalous vortex beam with self-focusing properties. Opt. Express 32 (22), 39429–39445. http://dx.doi.org/10.1364/OE.538458, URL https://opg.optica.org/oe/abstract.cfm?URI=oe-32-22-39429.

Allen, L., Beijersbergen, M.W., Spreeuw, R.J.C., Woerdman, J.P., 1992. Orbital angular momentum of light and the transformation of Laguerre-Gaussian laser modes. Phys. Rev. A 45, 8185–8189. http://dx.doi.org/10.1103/PhysRevA.45.8185, URL https://link.aps.org/doi/10.1103/PhysRevA.45.8185.

Anaya Carvajal, N., Acevedo, C.H., Torres Moreno, Y., 2017. Generation of perfect optical vortices by using a transmission liquid crystal spatial light modulator. Int. J. Opt. 2017 (1), 6852019. http://dx.doi.org/10.1155/2017/6852019, URL https://onlinelibrary.wiley.com/doi/abs/10.1155/2017/6852019.

Beržanskis, A., Matijošius, A., Piskarskas, A., Smilgevičius, V., Stabinis, A., 1998. Sum-frequency mixing of optical vortices in nonlinear crystals. Opt. Commun. 150 (1), 372–380. http://dx.doi.org/10.1016/S0030-4018(97)00591-9, URL https://www.sciencedirect.com/science/article/pii/S0030401897005919.

Chen, Y., Fang, Z.-X., Ren, Y.-X., Gong, L., Lu, R.-D., 2015. Generation and characterization of a perfect vortex beam with a large topological charge through a digital micromirror device. Appl. Opt. 54 (27), 8030–8035. http://dx.doi.org/10.1364/AO.54.008030, URL https://opg.optica.org/ao/abstract.cfm?URI=ao-54-27-8030.

Das, B.K., Ciappina, M.F., Gao, W., Granados, C., 2025a. High-harmonic generation driven by anomalous vortex beams. J. Phys. D: Appl. Phys. 58 (47), 475106. http://dx.doi.org/10.1088/1361-6463/ae1e0c.

Das, B.K., Granados, C., Ciappina, M.F., 2024. Generation of elliptical perfect optical vortex beams and their propagation in free-space. Appl. Opt. 63 (10), 2737–2745. http://dx.doi.org/10.1364/AO.521826, URL https://opg.optica.org/ao/abstract.cfm?URI=ao-63-10-2737.

Das, B.K., Granados, C., Ciappina, M.F., 2025b. Elliptical perfect optical vortex beam: Fourier transform of the asymptotic elliptical Laguerre–Gaussian beam. Opt. Commun. 577, 131417. http://dx.doi.org/10.1016/j.optcom.2024.131417, URL https://www.sciencedirect.com/science/article/pii/S0030401824011544.

Das, B.K., Granados, C., Ciappina, M.F., 2025c. Propagation of perfect optical vortex beams in a strongly nonlocal nonlinear medium. Results Opt. 21, 100842. http://dx.doi.org/10.1016/j.rio.2025.100842, URL https://www.sciencedirect.com/science/article/pii/S2666950125000707.

Das, B.K., Granados, C., Ciappina, M.F., 2025d. Propagation of modified anomalous vortex beams in a gradient-index medium. Opt. Commun. 591, 132030. http://dx.doi.org/10.1016/j.optcom.2025.132030, URL https://www.sciencedirect.com/science/article/pii/S0030401825005589.

Das, B.K., Granados, C., Ciappina, M., 2026. Optical vortices: revolutionizing the field of linear and nonlinear optics. Adv. Phys.: X 11 (1), 2608076. http://dx.doi.org/10.1080/23746149.2025.2608076.

Das, B.K., Krüger, M., Ciappina, M.F., 2025e. Second-harmonic generation in a KTP crystal driven by vortex beams with integer topological charges. In: Yue, Y. (Ed.), Second International Academic Conference on Optics and Photonics. IACOP 2024, Vol. 13541, International Society for Optics and Photonics, SPIE, 1354106. http://dx.doi.org/10.1117/12.3060305.

de las Heras, A., Schmidt, D., Román, J.S., Serrano, J., Barolak, J., Ivanic, B., Clarke, C., Westlake, N., Adams, D.E., Plaja, L., Durfee, C.G., Hernández-García, C., 2024. Attosecond vortex pulse trains. Optica 11 (8), 1085–1093. http://dx.doi.org/10.1364/OPTICA.517702, URL https://opg.optica.org/optica/abstract.cfm?URI=optica-11-8-1085.

Dholakia, K., Simpson, N.B., Padgett, M.J., Allen, L., 1996. Second-harmonic generation and the orbital angular momentum of light. Phys. Rev. A 54, R3742–R3745. http://dx.doi.org/10.1103/PhysRevA.54.R3742, URL https://link.aps.org/doi/10.1103/PhysRevA.54.R3742.

Fickler, R., Campbell, G., Buchler, B., Lam, P.K., Zeilinger, A., 2016. Quantum entanglement of angular momentum states with quantum numbers up to 10,010. Proc. Natl. Acad. Sci. 113 (48), 13642–13647. http://dx.doi.org/10.1073/pnas.1616889113, URL https://www.pnas.org/doi/abs/10.1073/pnas.1616889113.

Gariepy, G., Leach, J., Kim, K.T., Hammond, T.J., Frumker, E., Boyd, R.W., Corkum, P.B., 2014. Creating high-harmonic beams with controlled orbital angular momentum. Phys. Rev. Lett. 113, 153901. http://dx.doi.org/10.1103/PhysRevLett.113.153901, URL https://link.aps.org/doi/10.1103/PhysRevLett.113.153901.

Gradshteyn, I.S., Ryzhik, I.M., 2007. Table of Integrals, Series and Products (Seventh Edition). Elsevier.

Guo, Z., Chang, Z., Meng, J., An, M., Jia, J., Zhao, Z., Wang, X., Zhang, P., 2022. Generation of perfect optical vortex by Laguerre–Gauss beams with a high-order radial index. Appl. Opt. 61 (17), 5269–5273. http://dx.doi.org/10.1364/AO.461251, URL https://opg.optica.org/ao/abstract.cfm?URI=ao-61-17-5269.

He, J., Wan, M., Zhang, X., Yuan, S., Zhang, L., Wang, J., 2022. Generating ultraviolet perfect vortex beams using a high-efficiency broadband dielectric metasurface. Opt. Express 30 (4), 4806–4816. http://dx.doi.org/10.1364/OE.451218, URL https://opg.optica.org/oe/abstract.cfm?URI=oe-30-4-4806.

Kong, F., Zhang, C., Bouchard, F., Li, Z., Brown, G.G., Ko, D.H., Hammond, T.J., Arissian, L., Boyd, R.W., Karimi, E., Corkum, P.B., 2017. Controlling the orbital angular momentum of high harmonic vortices. Nat. Commun. 8 (1), 14970. http://dx.doi.org/10.1038/ncomms14970.

Kovalev, A.A., Kotlyar, V.V., Porfirev, A.P., 2016. Optical trapping and moving of microparticles by using asymmetrical Laguerre–Gaussian beams. Opt. Lett. 41 (11), 2426–2429. http://dx.doi.org/10.1364/OL.41.002426, URL https://opg.optica.org/ol/abstract.cfm?URI=ol-41-11-2426.

Kumar Das, B., Granados Buitrago, C., Ciappina, M.F., 2025d. Propagation of perfect optical vortex beams in a chiral medium. J. Opt. 27 (7), 075603. http://dx.doi.org/10.1088/2040-8986/ade815.

Li, Y., Zhou, Z.-Y., Ding, D.-S., Shi, B.-S., 2015. Sum frequency generation with two orbital angular momentum carrying laser beams. J. Opt. Soc. Am. B 32 (3), 407–411. http://dx.doi.org/10.1364/JOSAB.32.000407, URL https://opg.optica.org/josab/abstract.cfm?URI=josab-32-3-407.

Liu, L., Gao, Y., Liu, X., 2019. High-dimensional vortex beam encoding/decoding for high-speed free-space optical communication. Opt. Commun. 452, 40–47. http://dx.doi.org/10.1016/j.optcom.2019.06.061, URL https://www.sciencedirect.com/science/article/pii/S003040181930570X.

Liu, X., Li, Y., Yao, G., Li, C., Fang, B., Tang, Y., Hong, Z., Jing, X., 2024. Perfect vortex beams generation based on reflective geometric phase metasurfaces. Chinese J. Phys. 91, 828–837. http://dx.doi.org/10.1016/j.cjph.2024.08.028, URL https://www.sciencedirect.com/science/article/pii/S0577907324003289.

Ma, X., Zhang, H., Wei, W., Tai, Y., Qian, Y., Li, X., Shen, Y., 2026. Observation of superoscillation moiré superlattices. Adv. Photonics 8 (2), 026008. http://dx.doi.org/10.1117/1.AP.8.2.026008.

Ng, J., Lin, Z., Chan, C.T., 2010. Theory of optical trapping by an optical vortex beam. Phys. Rev. Lett. 104, 103601. http://dx.doi.org/10.1103/PhysRevLett.104.103601, URL https://link.aps.org/doi/10.1103/PhysRevLett.104.103601.

Ni, Y., Zhou, G., 2013. Propagation of a Lorentz–Gauss vortex beam through a paraxial ABCD optical system. Opt. Commun. 291, 19–25. http://dx.doi.org/10.1016/j.optcom.2012.11.016, URL https://www.sciencedirect.com/science/article/pii/S0030401812012886.

Ostrovsky, A.S., Rickenstorff-Parrao, C., Arrizón, V., 2013. Generation of the "perfect" optical vortex using a liquid-crystal spatial light modulator. Opt. Lett. 38 (4), 534–536. http://dx.doi.org/10.1364/OL.38.000534, URL https://opg.optica.org/ol/abstract.cfm?URI=ol-38-4-534.

Padgett, M., Arlt, J., Simpson, N., Allen, L., 1996. An experiment to observe the intensity and phase structure of Laguerre–Gaussian laser modes. Am. J. Phys. 64 (1), 77–82. http://dx.doi.org/10.1119/1.18283.

Qi, T., Wang, D., Gao, W., 2022. Sum-frequency generation of ring-Airy beams. Appl. Phys. B 128, 67. http://dx.doi.org/10.1007/s00340-022-07786-y.

Rego, L., Dorney, K.M., Brooks, N.J., Nguyen, Q.L., Liao, C.-T., Román, J.S., Couch, D.E., Liu, A., Pisanty, E., Lewenstein, M., Plaja, L., Kapteyn, H.C., Murnane, M.M., Hernández-García, C., 2019. Generation of extreme-ultraviolet beams with time-varying orbital angular momentum. Science 364 (6447), eaaw9486. http://dx.doi.org/10.1126/science.aaw9486, URL https://www.science.org/doi/abs/10.1126/science.aaw9486.

Shao, W., Huang, S., Liu, X., Chen, M., 2018. Free-space optical communication with perfect optical vortex beams multiplexing. Opt. Commun. 427, 545–550. http://dx.doi.org/10.1016/j.optcom.2018.06.079, URL https://www.sciencedirect.com/science/article/pii/S0030401818305856.

Shao, G.-h., Wu, Z.-j., Chen, J.-h., Xu, F., Lu, Y.-q., 2013. Nonlinear frequency conversion of fields with orbital angular momentum using quasi-phase-matching. Phys. Rev. A 88, 063827. http://dx.doi.org/10.1103/PhysRevA.88.063827, URL https://link.aps.org/doi/10.1103/PhysRevA.88.063827.

Sun, M., Xu, Y., Liu, Y., Li, C., Xu, B., Wang, X., Shi, J., Zhan, Q., 2025. Single-shot common-path encoded coherent diffraction imaging with OAM multiplexing. Photon. Res. 13 (6), 1620–1630. http://dx.doi.org/10.1364/PRJ.554521, URL https://opg.optica.org/prj/abstract.cfm?URI=prj-13-6-1620.

Vaity, P., Rusch, L., 2015. Perfect vortex beam: Fourier transformation of a Bessel beam. Opt. Lett. 40 (4), 597–600. http://dx.doi.org/10.1364/OL.40.000597, URL https://opg.optica.org/ol/abstract.cfm?URI=ol-40-4-597.

Wang, S., Cheng, M., Yang, X., Xu, J., Yang, Y., 2023. Self-focusing effect analysis of a perfect optical vortex beam in atmospheric turbulence. Opt. Express 31 (13), 20861–20871. http://dx.doi.org/10.1364/OE.492275, URL https://opg.optica.org/oe/abstract.cfm?URI=oe-31-13-20861.

Wang, B., Shi, J., Zhang, T., Xu, X., Cao, Y., Li, X., 2017. Improved lateral resolution with an annular vortex depletion beam in STED microscopy. Opt. Lett. 42 (23), 4885–4888. http://dx.doi.org/10.1364/OL.42.004885, URL https://opg.optica.org/ol/abstract.cfm?URI=ol-42-23-4885.

Xie, C., Giust, R., Jukna, V., Furfaro, L., Jacquot, M., Lacourt, P.-A., Froehly, L., Dudley, J., Couairon, A., Courvoisier, F., 2015. Light trajectory in Bessel-Gauss vortex beams. J. Opt. Soc. Amer. A 32 (7), 1313–1316. http://dx.doi.org/10.1364/JOSAA.32.001313, URL https://opg.optica.org/josaa/abstract.cfm?URI=josaa-32-7-1313.

Xu, F., Wang, M., Qiao, C., Li, S., Wang, H., Su, X., 2025. Hybrid entanglement carrying orbital angular momentum. Sci. Bull. 70 (6), 876–881. http://dx.doi.org/10.1016/j.scib.2025.01.003, URL https://www.sciencedirect.com/science/article/pii/S2095927325000052.

Yang, X., Fan, M., Zhang, H., Liu, K., Hu, J., Tai, Y., Shen, Y., Li, X., 2026. Fractional orbital angular momentum sorting using wind spiral transformation. Nanophotonics 15 (8), e70086. http://dx.doi.org/10.1002/nap2.70086, URL https://onlinelibrary.wiley.com/doi/abs/10.1002/nap2.70086.

Yang, Q., Xie, Z., Zhang, M., Ouyang, X., Xu, Y., Cao, Y., Wang, S., Zhu, L., Li, X., 2022. Ultra-secure optical encryption based on tightly focused perfect optical vortex beams. Nanophotonics 11 (5), 1063–1070. http://dx.doi.org/10.1515/nanoph-2021-0786.

Yuan, Y., Cong, Z., Gao, Y., Li, J., Zhao, Y., Hoenders, B.J., Cai, Y., Zhang, H., 2025. Optical encryption via four operations of orbital angular momentum. APL Photonics 10 (7), 076113. http://dx.doi.org/10.1063/5.0250395.

Zhang, S., Hou, W., Tao, X., Guo, M., Li, Y., Li, P., 2023. Second-harmonic generation of the vortex beams with integer and fractional topological charges. Photonics 10 (8), http://dx.doi.org/10.3390/photonics10080867, URL https://www.mdpi.com/2304-6732/10/8/867.

Zhang, H., Li, X., Ma, H., Tang, M., Li, H., Tang, J., Cai, Y., 2019. Grafted optical vortex with controllable orbital angular momentum distribution. Opt. Express 27 (16), 22930–22938. http://dx.doi.org/10.1364/OE.27.022930, URL https://opg.optica.org/oe/abstract.cfm?URI=oe-27-16-22930.

Zhao, S., Zhang, W., Wang, L., Li, W., Gong, L., Cheng, W., Chen, H., Gruska, J., 2019. Propagation and self-healing properties of Bessel-Gaussian beam carrying orbital angular momentum in an underwater environment. Sci. Rep. 9, http://dx.doi.org/10.1038/s41598-018-38409-2.

Zheng, G., Wu, Q., He, T., Zhang, X., 2022. Propagation characteristics of circular airy vortex beams in a uniaxial crystal along the optical axis. Micromachines 13 (7), http://dx.doi.org/10.3390/mi13071006, URL https://www.mdpi.com/2072-666X/13/7/1006.

Zhou, G., 2014. Beam propagation factors and kurtosis parameters of a Lorentz-Gauss vortex beam. J. Opt. Soc. Amer. A 31 (6), 1239–1246. http://dx.doi.org/10.1364/JOSAA.31.001239, URL https://opg.optica.org/josaa/abstract.cfm?URI=josaa-31-6-1239.

Zhou, Z.-Y., Ding, D.-S., Jiang, Y.-K., Li, Y., Shi, S., Wang, X.-S., Shi, B.-S., 2014. Orbital angular momentum light frequency conversion and interference with quasi-phase matching crystals. Opt. Express 22 (17), 20298–20310. http://dx.doi.org/10.1364/OE.22.020298, URL https://opg.optica.org/oe/abstract.cfm?URI=oe-22-17-20298.